Supporting Information

Polyoxometalate-based metal-organic framework-derived bimetallic hybrid materials for upgraded electrochemical reduction of nitrogen

Xinming Wang[‡a], Zemin Feng[‡a], Boxin Xiao[a], Jingxiang Zhao[b], Huiyuan Ma*[a], Yu Tian*[c], Haijun Pang[a], and Lichao Tan[a]

[a]College of Chemical and Environmental Engineering, Harbin University of Science and Technology, Harbin 150040, P. R. China. E-mail address: mahy017@163.com

[b]College of Chemistry and Chemical Engineering, and Key Laboratory of Photonic and Electronic Bandgap Materials, Ministry of Education, Harbin Normal University, Harbin, 150025, P. R. China.

[c]Institute for Interdisciplinary Quantum Information Technology, Jilin Engineering Normal University, Changchun, 130052, Jilin, P. R. China. E-mail address: tiany@jlenu.edu.cn

[‡]Xinming Wang and Zemin Feng contributed equally to this work.

Experimental Methods:

1. Chemicals and Materials

All reagents for syntheses were purchased commercially and used as received without further purification. Polyvinylpyrrolidone K30 (PVP) were purchased from Sinpharm Chemical Reagent Co..ltd. Iron chloride hexahydrate ($FeCl_3 \cdot 6H_2O$, 99.0%), trimesic acid ($C_6H_3(CO_2H)_3$, 99.0%), phosphomolybdic acid tetracosahydrate ($H_3PMo_{12}O_{40} \cdot 24H_2O$, 99.0%), thiourea ($H_2NCSNH_2$, 99.0%), potassium hydroxide (KOH, AR), ammonium chloride (NH_4Cl, 99.5%), iso-propyl alcohol (C_3H_8O, 99.5%), Nafion perfluorinated resin solution, potassium sulfate (K_2SO_4, 99.0%), p-dimethylaminobenzaldehyde ($C_9H_{11}NO$, 99%), potassium chloride (KCl, 99.5%), potassium iodide (KI, 99.5%), mercuric iodide (HgI, 99.5%), sodium hydroxide (NaOH, 96.0%), sulfuric acid (H_2SO_4, 95.0~98.0%), potassium sodium tartrate tetrahydrate ($C_4H_{12}KNaO_{10}$, 99.0%), hydrazine monohydrate ($N_2H_4 \cdot H_2O$, 99.0%), and ethanol (C_2H_6O, 75%) were obtained from Beijing Chemical Works, China. $(NH_4)_2SO_4$ with the ^{15}N enrichment of 98% were obtained from Sigma-Aldrich, USA. Dimethyl sulfoxide-d6 (DMSO-d_6, deuterium for 99.9%) were obtained from Alfa Aesar, USA. Nitrogen (N_2, high-purity, 99.9999%) and argon (Ar, high-purity, 99.9999%) were purchased from Qing Hua Gas Co., China. The $^{15}N_2$ isotope with the N enrichment of 99% was obtained from Shanghai Research Institute of Chemical Industry Co., China. The carbon cloth (CC) was purchased from CeTech Co., Ltd and was pretreated in HNO_3, then was cleaned by sonication sequentially in acetone, H_2O, and C_2H_5OH several times to remove the surface impurities. Ultrapure water (18.2 MΩ cm) was used in all experiments.

2. Characterization

The FI-IR spectra were recorded from KBr pellets in the range of 4000–400 cm^{-1} with a Bruker Tensor II spectrometer (Bruker, Germany). The powder X-ray diffraction (PXRD) patterns were obtained with a Rigaku D/max 2500 V PC diffractometer with Cu-Kα radiation, and the scanning rate is 5°/s, 2θ ranging from 5 to 90°. X-ray phototelectron spectra (XPS) was measured with VG ESCALAB MK (VK Company, UK) at room temperature by using a Al Kα X-ray source at 12 KV and 20 mA. The surface structures and morphology of the samples were characterized by a field-emission scanning electron microscopy (FE-SEM) (Hitachi, SU8000) and transmission electron microscopy (TEM) (JEOL, JEM-2010, 200 kV). Energy dispersive spectroscopy (EDS) data was collected with an ensemble measurement in the FE-SEM. Raman spectra were recorded on a LabRAM HR Evolution micro-Raman spectrometer at room temperature using a 325 nm Ar^+ laser as the excitation source (HORIBA Scientific, France). ^1H nuclear magnetic resonance (NMR) experiments were carried out at 303 K for 5% w/v sample solution in DMSO-d_6 using Bruker Avance NEO 600. The spectral windows were set to 12.5 kHz (25 ppm), a total of 16 scans were recorded, a π/2 pulse length of 11.6 μs and 64 K data points

with 3 s recycle delay for each sample. After NRR test, the electrolyte was subjected to distillation treatment, and the steam including NH_3 and H_2O was condensed into a container. Solid product was then obtained for NMR examination by freeze-dring of above solution. UV-visible spectra were measured on a U-3900 UV–vis spectrophotometer (Hitachi, Japan). All the electrochemical tests were carried out in a three-electrode testing system (CHI 760E electrochemical workstation, Chenhua, Shanghai). A conventional three-electrode system was used, with the catalyst ink loaded commercial carbon cloth carbon (CC) as a working electrode, a commercial Ag/AgCl as reference electrode and platinum sheet as counter electrode.

3. Synthesis of Catalysts

3.1. Synthesis of PMo_{12}@MIL-100(Fe)@PVP

PMo_{12}@MIL-100(Fe)@PVP was prepared following the protocol described earlier with some changes.[1] Different amounts of PVP (0.8, 1.2, 1.6, 2.5 and 3.3 wt%) were calculated based on the total mass of starting solid materials including $FeCl_3 \cdot 6H_2O$, $H_3PMo_{12}O_{40} \cdot 24H_2O$ and trimethyl 1,3,5-benzenetricarboxylate. Take PMo_{12}@MIL-100(Fe)@PVP (1.6 wt%) for example, 50 mL of water solution consisting of $FeCl_3 \cdot 6H_2O$ (1.89 g), $H_3PMo_{12}O_{40} \cdot 24H_2O$ (1.35 g) and PVP (0.07 g) were thoroughly dissloved with ultrasonication. Then, trimethyl 1,3,5-benzenetricarboxylate (1.36 g) was added into the above solution. After being stirred for another 1 h, the resulting solution was transferred into a Teflon-lined stainless-steel autoclave with a capacity of 100 mL. The autoclave was sealed and heated at 130 °C for 72 h and naturally cooled to room temperature. The brown precursors were collected by centrifuging, washed several times with water and absolute ethanol, and finally dried in a vacuum oven at 60°C for 5 h.

3.2. Synthesis of MIL-100(Fe)@PVP (1.6 wt%)

In a typical synthesis, 50 mL of water solution consisting of $FeCl_3 \cdot 6H_2O$ (1.89 g), trimethyl 1,3,5-benzenetricarboxylate (1.36 g) and PVP (0.05 g) were thoroughly dissloved with ultrasonication. Subsequently, the solution was heated at 130 °C for 72 h in a 100 mL Teflon reactor and naturally cooled to room temperature. These brown precursors were collected by centrifuging, washed several times with water and absolute ethanol, and finally dried in a vacuum oven at 60°C for 5 h.

3.3. $Fe_{1.89}Mo_{4.11}O_7/FeS_2$@C Catalyst Preparation

Briefly, PMo_{12}@MIL-100(Fe)@PVP (0.1 g) and thiourea (0.4 g) were dissolved in deionized water (50 mL) by ultrasonication for 30 min to form a homogeneous suspension solution. Then, the solution was transferred into a 100 mL Teflon-lined stainless steel autoclave maintained at 160 °C for 6 h and then cooled to room temperature naturally. The final product (denote as $Fe_{1.89}Mo_{4.11}O_7/FeS_2$@C) were acid pickling with H_2SO_4 (0.5 M) to remove unstable and inactive species. The samples were then thoroughly washed with de-ionized water until reaching a neutral pH, and

were dried in a vacuum oven at 60 °C overnight.

Note: The distinction in the serial structure of $Fe_{1.89}Mo_{4.11}O_7/FeS_2$@C (0.8, 1.2, 1.6, 2.5 and 3.3 wt%) stems from the different amounts of PVP in the precursors.

3.4. $FeMoO_4/FeS_2$@C Catalyst Preparation

PMo_{12}@MIL-100(Fe)@PVP (1.6 wt%) (0.1 g) and thiourea (0.4 g) were dissolved in deionized water (50 mL) by ultrasonication for 30 min to form a homogeneous suspension solution. Then, the solution was transferred into a 100 mL Teflon-lined stainless steel autoclave maintained at 200 °C for 24 h and then cooled to room temperature naturally. The final product (denote as $FeMoO_4/FeS_2$@C) were acid pickling with H_2SO_4 (0.5 M) to remove unstable and inactive species. The samples were then thoroughly washed with de-ionized water until reaching a neutral pH, and were dried in a vacuum oven at 60 °C overnight.

3.5. FeS_2@C Catalyst Preparation

The obtained MIL-100(Fe)@PVP (1.6 wt%) precursors (0.1 g) and thiourea (0.4 g) were dissolved in deionized water (50 mL) by ultrasonication for 30 min to form a homogeneous suspension solution. Then, the solution was transferred into a 100 mL Teflon-lined stainless steel autoclave maintained at 200 °C for 24 h and then cooled to room temperature naturally. The final product (denote as FeS_2@C) were acid pickling with H_2SO_4 (0.5 M) to remove unstable and inactive species. The samples were then thoroughly washed with de-ionized water until reaching a neutral pH, and were dried in a vacuum oven at 60 °C overnight.

4. Electrochemical Measurements

4.1. NRR Cathode Preparation

A homogeneous ink for the electrochemical measurement was prepared by mixing 10 mg of the catalyst into 2.2 mL of deionized water and 750 μL isopropyl alcohol and 50 μL Nafion® solution (0.1 wt% water solution), followed by sonication for 60 min. The cathode was prepared by loading the ink onto a carbon cloth electrode (1 cm × 1 cm) and drying under ambient conditions with a loading of 0.3 mg cm^{-2}.

4.2. Electrochemical Measurement

NRR experiments were performed in a typical H-cell arrangement separated by a Nafion 211 membrane at room temperature. Before NRR test, Nafion membrane was protonated by first boiling in water for 1 h, then in H_2O_2 for 1 h, then in water for another hour, followed by 3 h in 0.5 M H_2SO_4, and finally for 6 h in water. All steps were performed at 80 °C.[2] The electrochemical measurements were conducted by a CHI 760 electrochemical analyzer (Shanghai, Chenhua Co., China) in a three-

electrode cell containing electrolyte. Typically, a synthesized catalyst/CC as working electrode, an Ag/AgCl (in saturated KCl electrolyte) electrode was used as the reference electrode and a platinum foil electrode (2 cm × 2 cm) as the counter electrode. The potentials reported in this work were converted to RHE scale via calibration with the following equation: E (vs RHE) =E (vs Ag/AgCl) + 0.197 + 0.059 × pH, and the polarization curves were the steady-state ones after several cycles. The presented current density referred to the geometrical area of the CC. Before all measurements, high-purity Ar and N_2 were first bubbled into the cathode compartment for at least 30 min with a constant flow rate of 150 mL min^{-1} to remove air in electrolyte and reactor, and then a constant flow rate of 25 mL min^{-1} was maintained with a properly positioned sparger during the entire experimental process using a mass flow controller (LZB-3WB) purchased from MK precision Co, Ltd.. For NRR tests, a potentiostatic test was conducted for 2 h in an N_2-saturated acidic potassium sulfate (pH 3.5, 1.0 mol L^{-1} of K^+) or 0.1 M KOH electrolytes (40 mL) at the ambient conditions of 298 K and 1 bar. Linear sweep voltammetry (LSV) measurements of the catalysts were conducted in Ar- and N_2-saturated acidic potassium sulfate (pH 3.5, 1.0 mol L^{-1} of K^+) solution between –1 and 0 V vs RHE with a scan rate of 10.0 mV s^{-1}. All polarization curves were obtained without current resistance (iR) compensation. Electrochemical impedance spectroscopy (EIS) measurements were carried out from 0.1 Hz to 1000 kHz with an amplitude of 10 mV at the open-circuit voltage. To estimate the electrochemical active surface areas (ESCAs) of the $Fe_{1.89}Mo_{4.11}O_7/FeS_2$@C, $FeMoO_4/FeS_2$@C and FeS_2@C, the double layer capacitance (C_{dl}) of the catalytic surface was measured with cyclic voltammetry (CV) in a Faradaic silence potential range of 0.15~0.35 V vs RHE, in an Ar-saturated acidic potassium sulfate (pH 3.5, 1.0 mol L^{-1} of K^+) solution using different scan rates (5~100 mV s^{-1}).

5. Procedures for the Determination of NH_3 or N_2H_4

5.1. Determination of NH_3 using Nessler′s Reagent Spectrophotometry

The concentration of produced NH_3 was determined via a UV-vis spectrophotometry according to Chinese National Standard method HJ 535-2009 using Nessler′s reagent as a chromogenic agent at 420 nm with a light path of 1 cm.[3] First, 5 mL of the sample was taken into the colorimetric tubes and made up to 10 mL with acidic potassium sulfate (pH 3.5, 1.0 mol L^{-1} of K^+) or 0.1 M KOH. Next, 1 mL of 0.2 M potassium sodium tartrate ($KNaC_4H_4O_6$) was added and mixed thoroughly to chelate interfering soluble metalions. Third, 1 mL of Nessler′s reagent was added to

stand for 30 minutes for color development, and the absorbance of the resulting solution was recorded at 420 nm. The blank control was used 5 mL of the electrolyte solution instead of the sample. Calibration curve of NH_3 in electrolyte solution was plotted using a series of different concentration of standard ammonia stock solution diluted by acidic potassium sulfate (pH 3.5, 1.0 mol L^{-1} of K^+) or 0.1 M KOH. The linear relationship was $y = 0.19276x + 0.00229$, $R^2 = 0.9990$ and $y = 0.1777x + 0.0014$, $R^2 = 0.9995$ in acidic and basic electrolytes, respectively.

The Faradaic efficiency (FE) and mass normalized yield of NH_3 were calculated using the following equation:

NH_3 yield = $c_{NH_3} \times V/(m_{cat.} \times t)$ (1)

The rate of NH_3 formation was calculated as Equation 1, where c_{NH_3} was the total mass concentration of NH_3, V was the volume of the electrolyte, t was the reduction reaction time, and $m_{cat.}$ is the loaded quality of catalyst.

Faradaic efficiency (FE) was calculated according to the following equation:

$FE = 3 \times F \times c_{NH_3} \times V/(17 \times Q)$ (2)

Considering that assuming three electrons were needed to produce one NH_3 molecule, the Faradaic efficiency (FE) for NRR was calculated as Equation 2, Where c_{NH_3} was the total mass concentration of NH_3, V is the volume of the cathodic reaction electrolyte, F was the Faraday constant, and Q was the charge.

The electrochemical double-layer capacitance (C_{dl}) of the materials was measured to determine their electrochemical surface area (ECSA) using the cyclic voltammograms (CVs) in a small potential range with no faradic processes between 0.2 and 0.3 V vs. RHE. The plotted current density against scan rate has a liner relationship and its slope is twice the C_{dl}. The ECSA can then be calculated as below:

$A_{ECSA} = C_{dl}$ of catalyst (mF cm^{-2})/40 μF cm^{-2} per cm_{ECSA}^2 (3)

The surface-area-normalized activity of NH_3 was calculated as below:

NH_3 $Yield_{ECSA} = c_{NH_3} \times V/(A_{ECSA} \times t)$ (4)

5.2. Determination of N_2H_4 Using the Watt and Chrisp Method

The production of N_2H_4 in the electrolyte was estimated by the Watt and Chrisp method.[4] The mixture of para-(dimethylamino) benzaldehyde (5.99 g), HCl (concentrated, 30 mL) and ethanol (300 mL) was used as a color reagent. 5 mL of the electrolyte sample was made up to 10 mL with acidic potassium sulfate (pH 3.5, 1.0 mol L^{-1} of K^+). Then 5 mL above prepared color reagent was added with stirring 20 min at room temperature. Absorbance of the resulting solution was measured at 460 nm. The blank control was used 5 mL of the electrolyte instead of the sample. Calibration curve of N_2H_4 in acidic potassium sulfate (pH 3.5, 1.0 mol L^{-1} of K^+) was

plotted using a series of different concentration of standard N_2H_4 stock solution diluted by acidic potassium sulfate (pH 3.5, 1.0 mol L^{-1} of K^+). The fitting curve shows good linear relation of absorbance with N_2H_4 concentration. The linear relationship was $y = 1.27655x - 0.022$, $R^2 = 0.9991$

6. The Control Experiments for the Investigations of Ammonia Contamination and Nitrogen Source

6.1. The Ammonia Contribution of the Supplied Nitrogen Gas

In the three-electrode H-cell containing electrolyte, 40 mL of acidic potassium sulfate electrolytes (pH 3.5, 1.0 mol L^{-1} of K^+) electrolyte was bubbled with nitrogen gas ((N_2, high-purity, 99.9999%)) 2 hours with a constant flow rate of 25 mL min^{-1} and then was analyzed using Nessler′s reagent. The result was out of the quantitatively linear range (Figure S30a).

6.2. The Ammonia Contribution of the Cathode without Catalyst

The measurement was conducted under the same condition with the electrochemical NRR procedure using 2.2 mL deionized water, 750 μL isopropyl alcohol and 50 μL Nafion solution, respectively. The deionized water, isopropyl alcohol and Nafion solution were all dispersed on a bare carbon cloth electrode at –0.4 V vs RHE for 2 h and then was analyzed using Nessler′s reagent respectively. The result was all out of the quantitatively linear range (Figure S30b-S30d).

6.3. The Ammonia Contribution of the Impurities from Catalysts

The measurement was conducted under the same condition with the electrochemical NRR procedure at open circuit potential for 2 h and then was analyzed using Nessler′s reagent. The result was out of the quantitatively linear range (Figure S30e).

6.4. The Control Experiments Performing in an Ar Atmosphere

The control experiment for the electrochemical NRR procedure was conducted under 2 h electrolysis with an applied potential at –0.4 V vs RHE in 40 mL of acidic potassium sulfate electrolytes (pH 3.5, 1.0 mol L^{-1} of K^+) electrolyte except using Ar gas instead (Figure S30f). The result was out of the quantitatively linear range.

6.5. The Control Experiments of the $^{15}N_2$ Isotopic Measurements to Prove the Nitrogen Source

The ^{15}N isotopic measurements were performed using the $^{15}N_2$ isotope with the ^{15}N (enrichment of ＞99%) to clarify the nitrogen origination of ammonia (Figure S32). Before the electrochemical reduction procedure, the electrolyte (pH 3.5, 1.0 mol L^{-1} of K^+) was purged with high-purity Ar to remove the ^{14}N from solution and then

was pre-saturated with $^{15}N_2$ for 30 min with a flow rate of 10 mL min^{-1} (A low-velocity gas flow was adopted due to the limited supply and expense of $^{15}N_2$). After 10 h electrolysis at –0.4 V vs. RHE, the 10 mL of the electrolyte was taken out and adjusted to pH = 3. The analysis of $^{15}NH_3$ product was conducted by the ^1H nuclear magnetic resonance with water suppression (^1H NMR, Bruker Avance NEO 600).

7. Computational Methods and Models

All of the DFT calculations were performed by using Vienna ab initio simulation pachage (VASP).[5,6] The exchange–correlation energy is treated based on the generalized gradient approximation (GGA) in the scheme of Perdew–Burke–Ernzerhof (PBE).[7] The core–electron interactions are describe by Projector–augmented–wave (PAW) pseudopotentials.[8] To describe the van der Waals (vdW) interaction in the systems properly, DFT with the empirical dispersion correction (DFT–D3) method is applied due to its good description of long–range vdW interactions.[9] The $Fe_{1.89}Mo_{4.11}O_7/FeS_2$, $Fe_{1.89}Mo_{4.11}O_7$ (002), and FeS_2 (200) surfaces observed in the experiment were modeled with 15 Å of vacuum to avoid the unwanted interaction between the slab and its period images. During the geometry optimization, the atoms on the bottom two layers were fixed in their bulk positions, whereas the atoms on the two top layers and all adsorbates were allowed to relax. A 4 × 4 × 1, 4× 4 × 1, and 5× 5× 1 Monkhorst–Pack k–point grid were adopted for calculations on $Fe_{1.89}Mo_{4.11}O_7/FeS_2$, $Fe_{1.89}Mo_{4.11}O_7$ (002), and FeS_2 (200), respectively. The energy cutoff is set to be 420 eV. All atoms were fully relaxed until the total energy converges to less than 10^{-4} eV and the ionic relaxation were performed until the force on each atom converge to within 0.02 eV $Å^{-1}$.

The free–energy change (ΔG) of each elementary reaction step on these electrocatalysts was calculated according to the computational hydrogen electrode (CHE) model suggested by Nørskov et al..[10,11] According to this method, the reaction free energies of the NRR steps were calculated as: $\Delta G = \Delta E + \Delta E_{ZPE} - T\Delta S + \Delta G_U + \Delta G_{pH}$, where ΔE is the electronic energy difference directly obtained from DFT calculations, ΔE_{ZPE} is the change in zero–point energies, T is the temperature (T = 298.15 K), and ΔS is the entropy change. The entropies and vibrational frequencies of molecules in the gas phase were taken from the NIST database,[12] while the vibrational frequencies of adsorbed species were computed to obtain ZPE contribution in the free energy expression.[13–15] Only adsorbate vibrational modes were computed explicitly, while the catalyst sheet was fixed (assuming that vibrations of the substrate are negligible). ΔG_U is the free energy contribution related to electrode potential U. ΔG_{pH}

is the correction of the H^+ free energy by the concentration, which can be determined as $\Delta G_{pH} = 2.303 \times k_B T \times pH$, where k_B is the Boltzmann constant and the value of pH was assumed to be zero.

Supplementary Figures and Tables

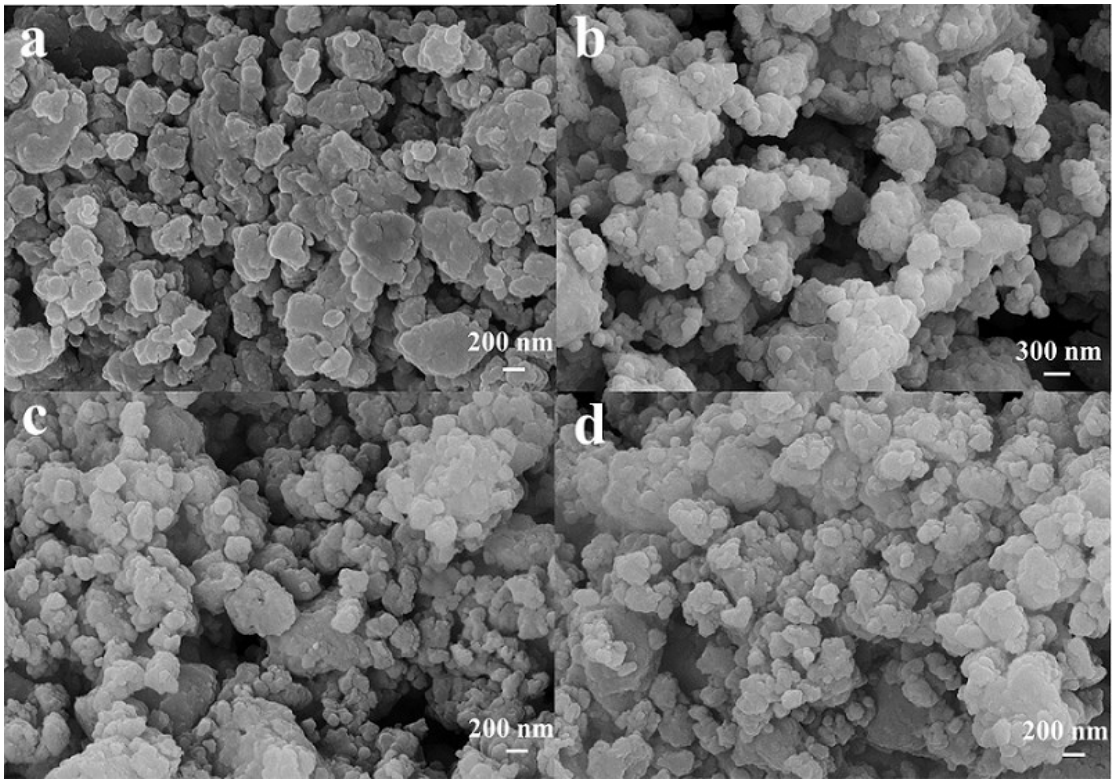

Figure S1. SEM images of $Fe_{1.89}Mo_{4.11}O_7/FeS_2$@C derived from the precursors with different amounts of PVP. (a) 0.8% PVP (b) 1.2% PVP (c) 2.5% PVP (d) 3.3% PVP

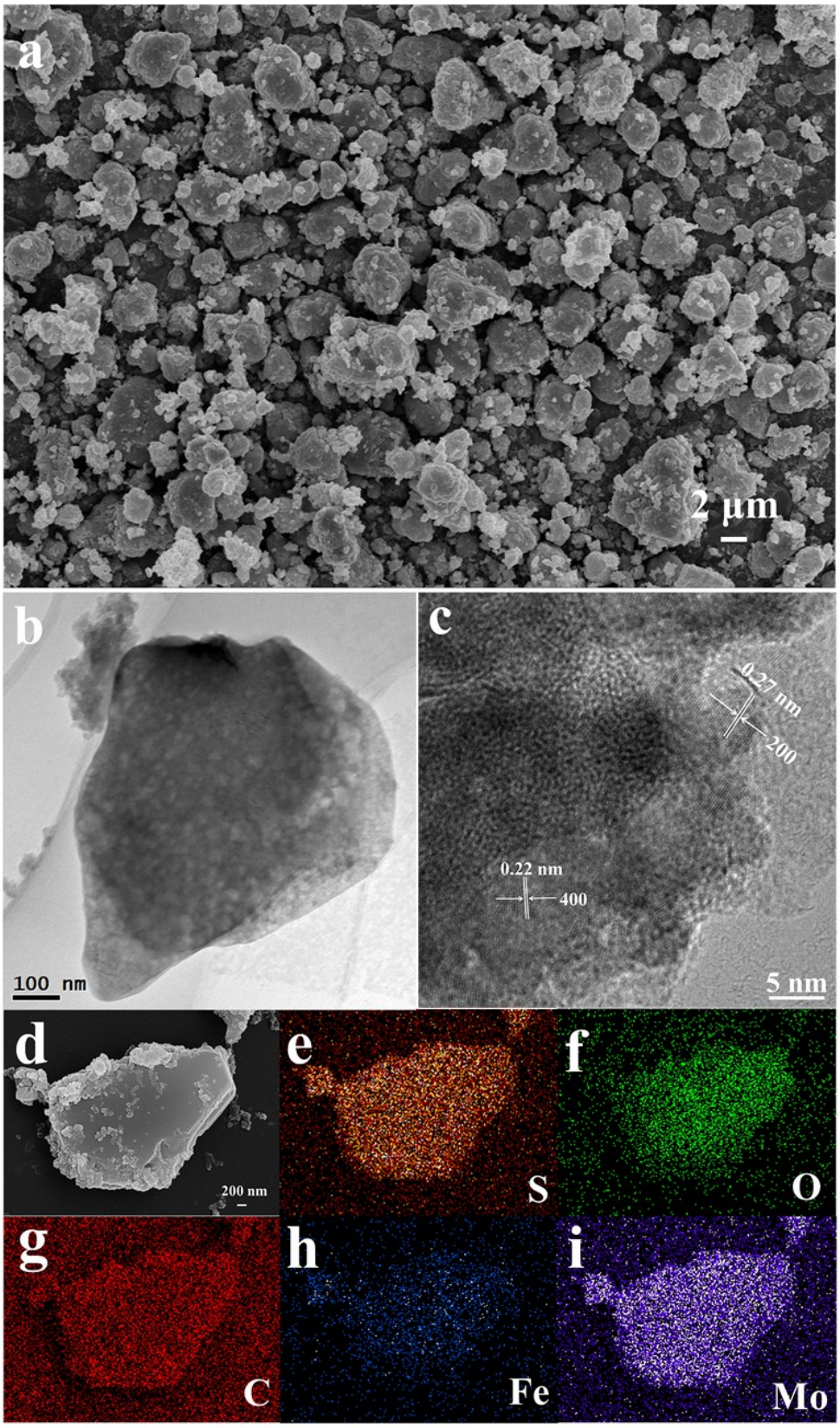

Figure S2. (a) SEM images for the as-prepared $FeMoO_4/FeS_2$@C. (b) TEM image of $FeMoO_4/FeS_2$@C (c) HRTEM image of $FeMoO_4/FeS_2$@C (d-i) Element mapping images of $FeMoO_4/FeS_2$@C including S, O, C, Fe, and Mo.

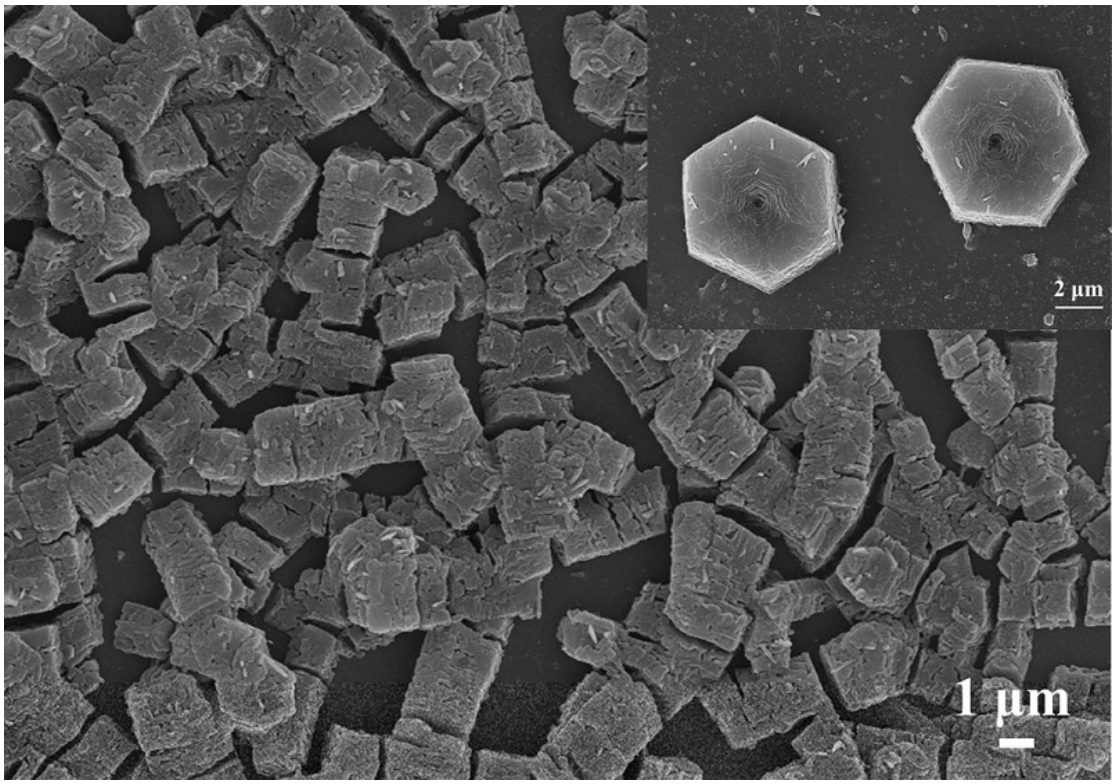

Figure S3. SEM of MIL-100(Fe)@PVP (1.6 wt%)

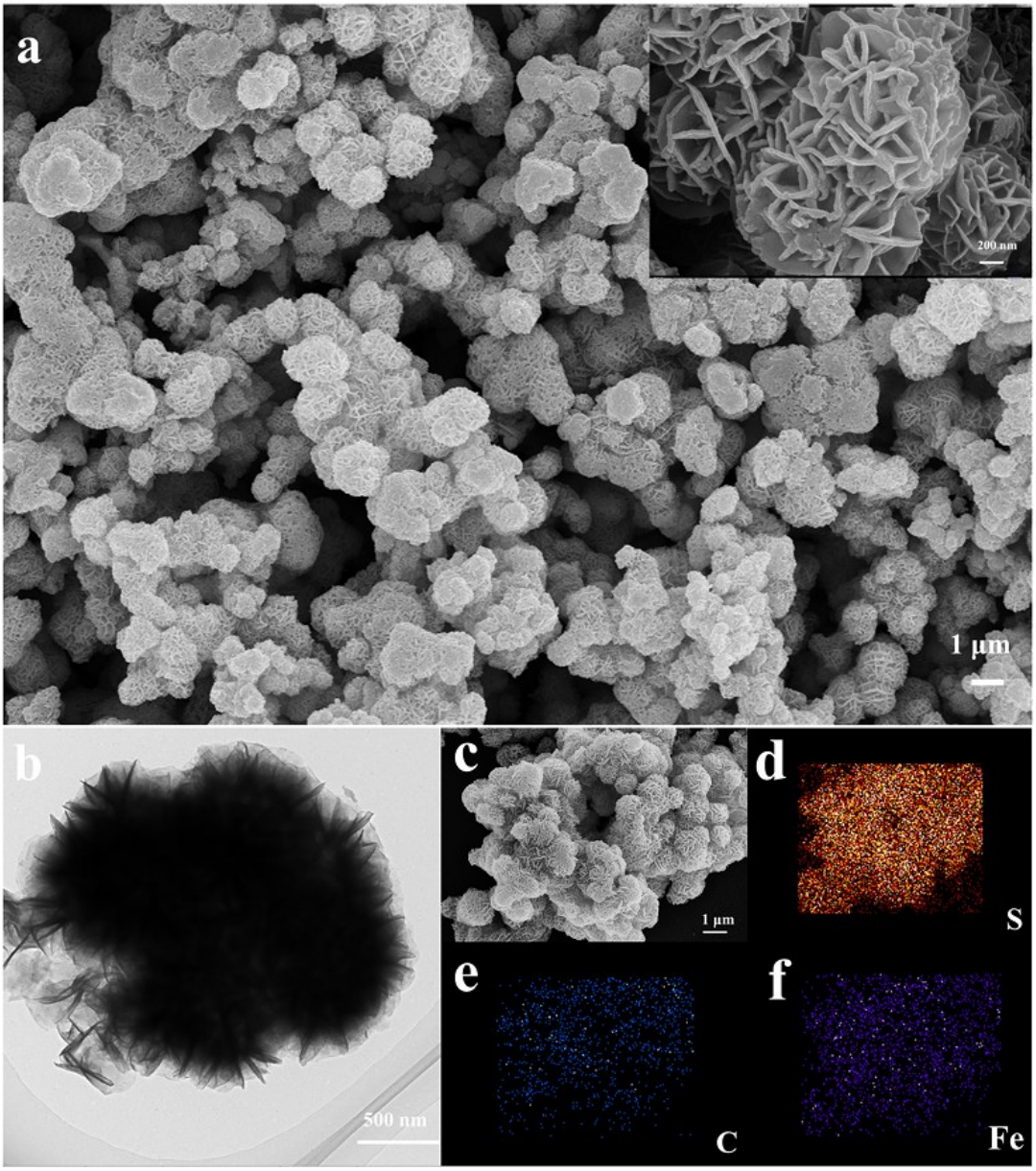

Figure S4. (a) SEM of FeS_2@C (b) HRTEM of FeS_2@C (c-f) Element mapping images of FeS_2@C, including S, C, and Fe.

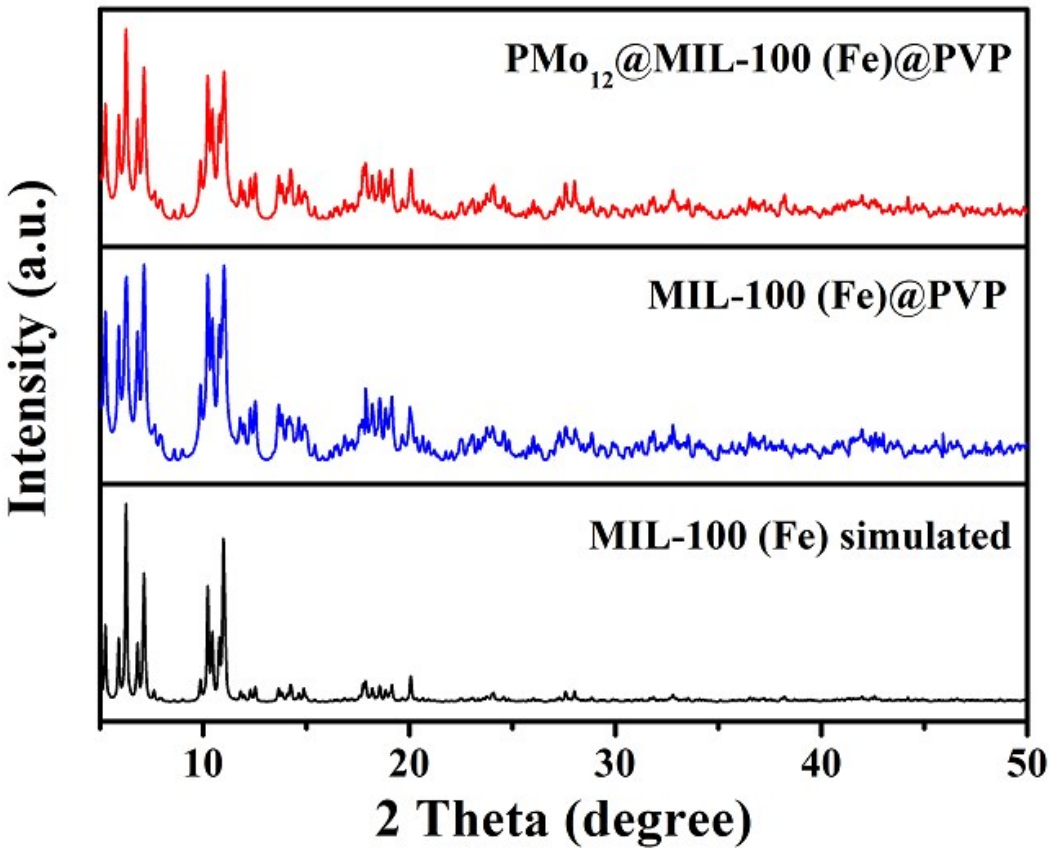

Figure S5. PXRD spectra of PMo_{12}@MIL-100(Fe)@PVP (1.6 wt%), MIL-100 (Fe)@PVP (1.6 wt%), and MIL-100(Fe) simulated.

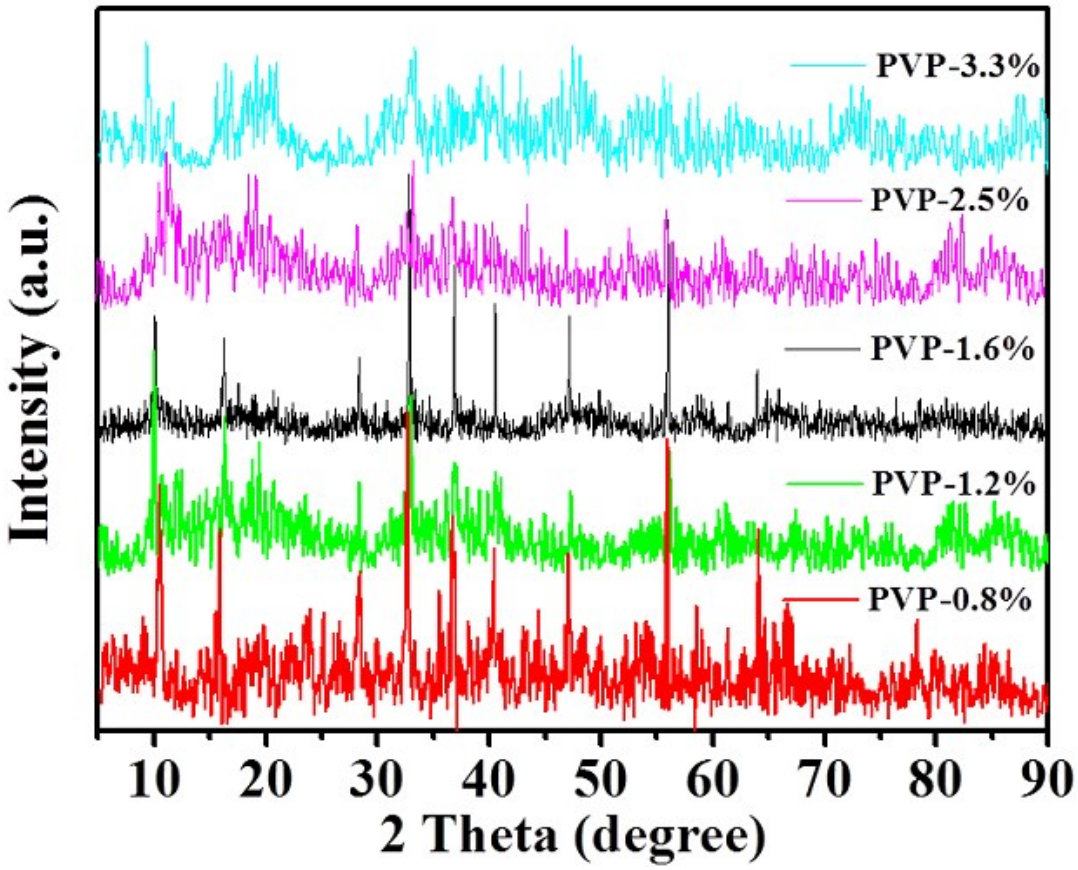

Figure S6. The comparative PXRD spectra of $Fe_{1.89}Mo_{4.11}O_7/FeS_2$@C with different amounts of PVP (0.8, 1.2, 1.6, 2.5, 3.3 wt%) in their precursors.

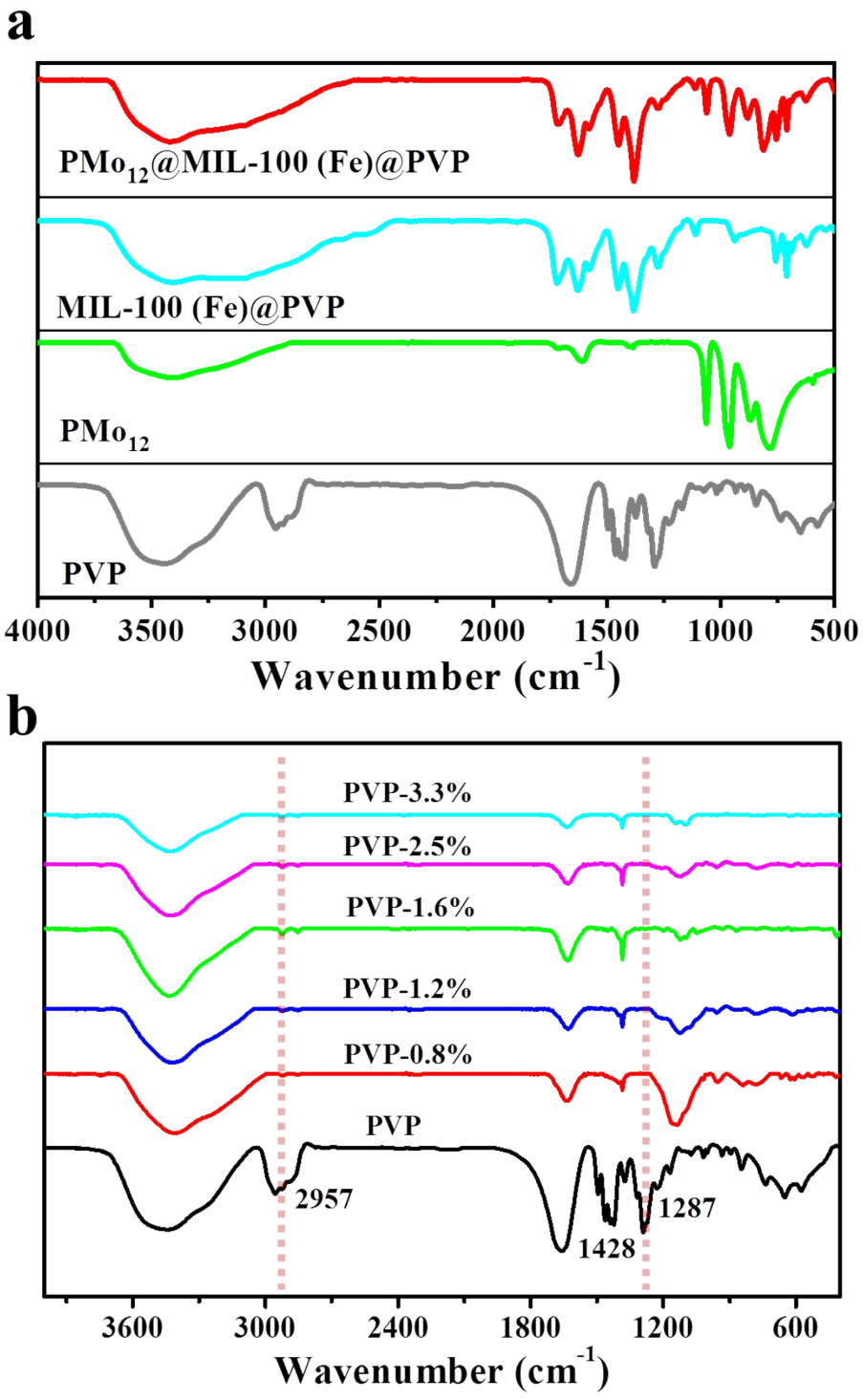

Figure S7. (a) IR spectra of as-synthesized PMo_{12}@MIL-100(Fe)@PVP (1.6 wt%), MIL-100(Fe)@PVP (1.6 wt%), PMo_{12}, and PVP. (b) IR spectra of PVP and $Fe_{1.89}Mo_{4.11}O_7/FeS_2$@C derived from the precursors with different amounts of PVP.

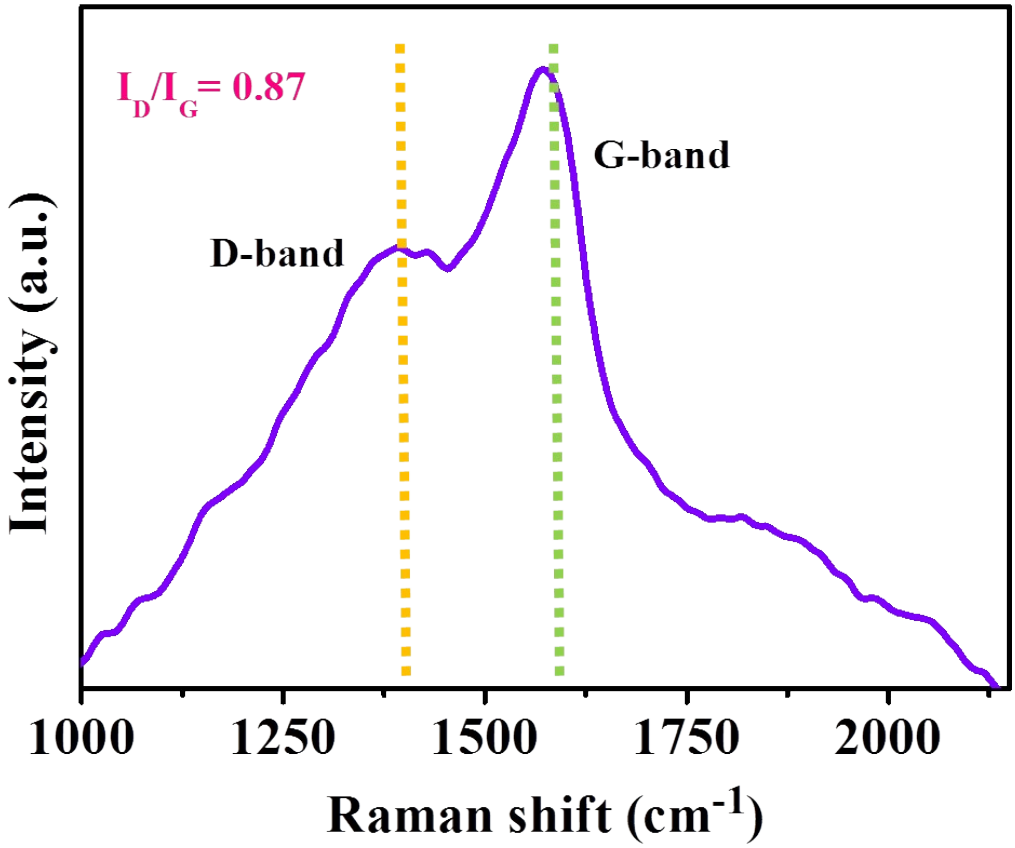

Figure S8. Raman spectra of $Fe_{1.89}Mo_{4.11}O_7/FeS_2$@C (1.6 wt%)

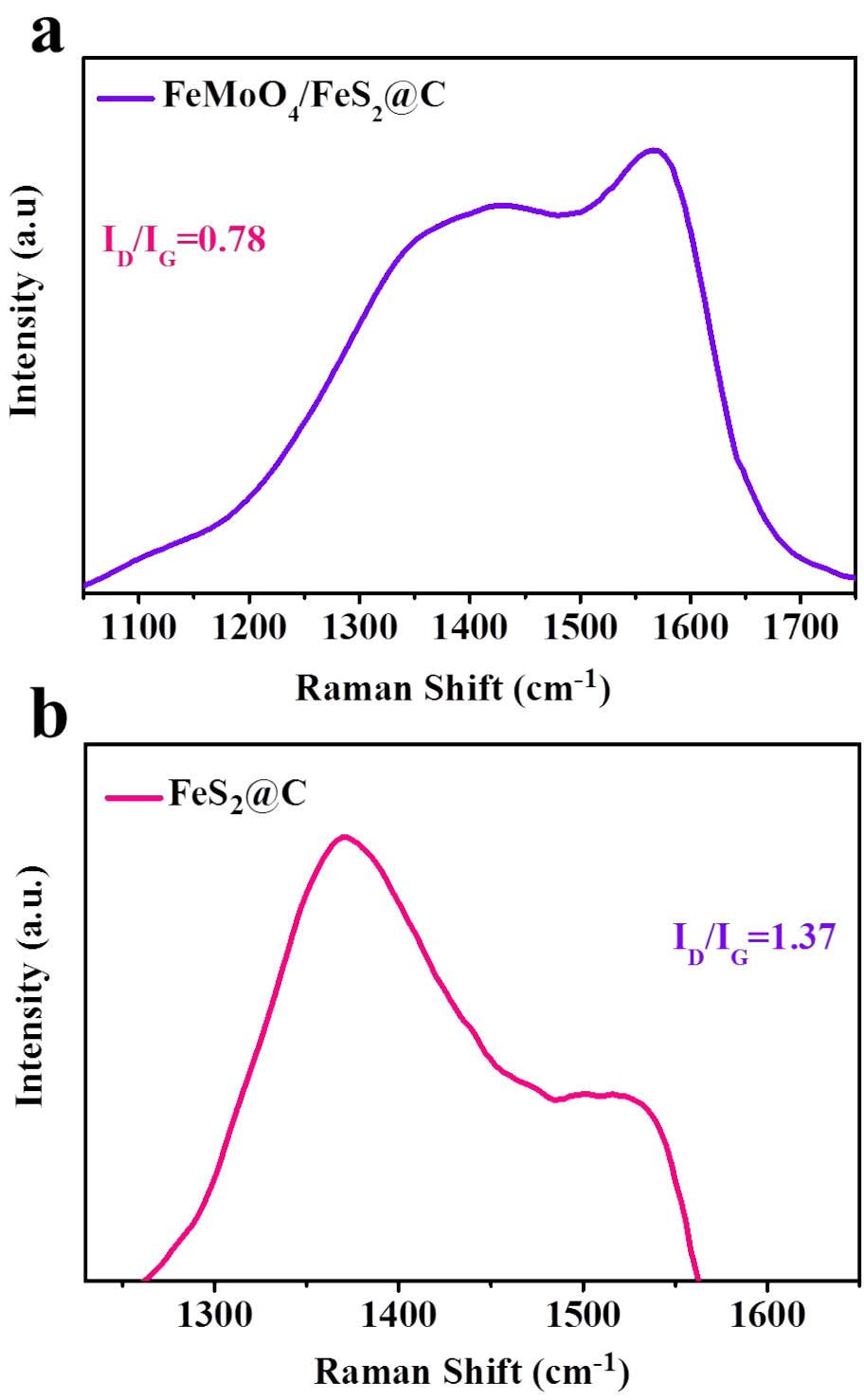

Figure S9. Raman spectra of $FeMoO_4/FeS_2$@C and FeS_2@C (that is all derived from the precursors with PVP 1.6 wt%).

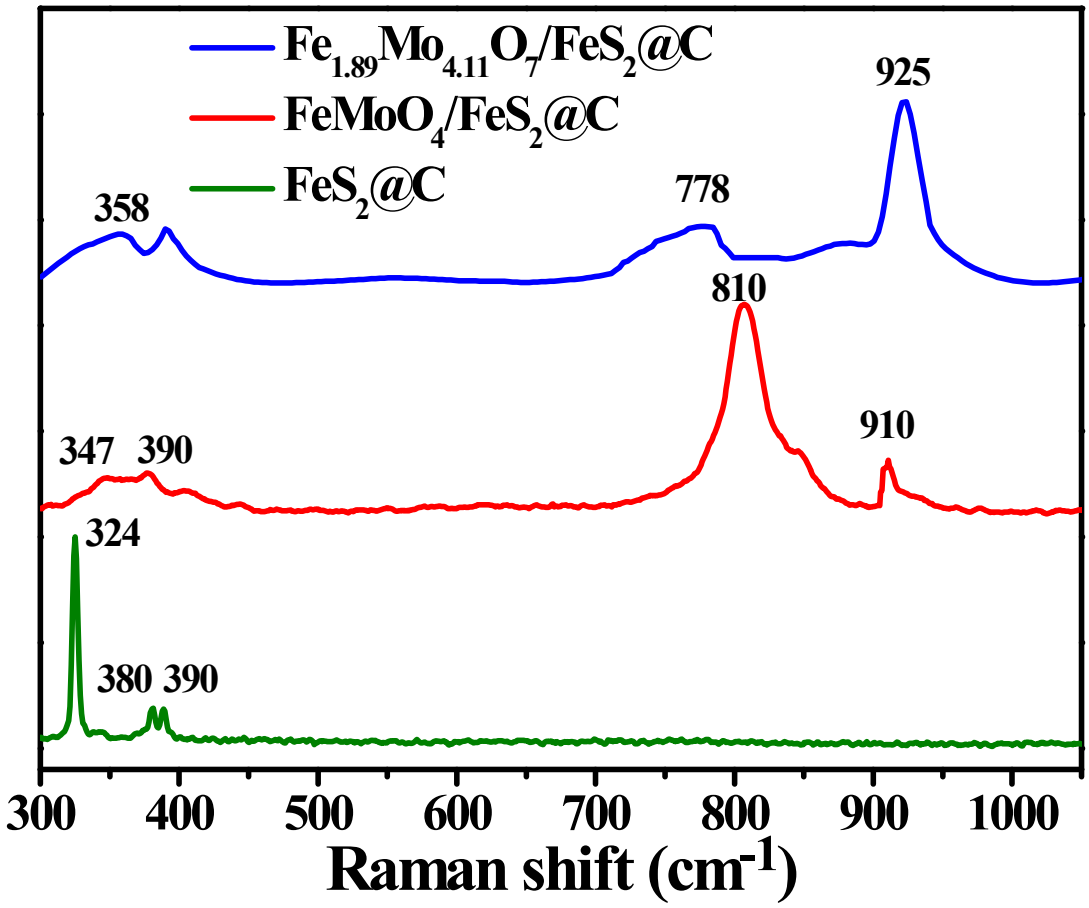

Figure S10. Raman spectra of $Fe_{1.89}Mo_{4.11}O_7/FeS_2$@C (1.6%), $FeMoO_4/FeS_2$@C and FeS_2@C. The excitation wavelength is 325 nm from an Ar ion laser.

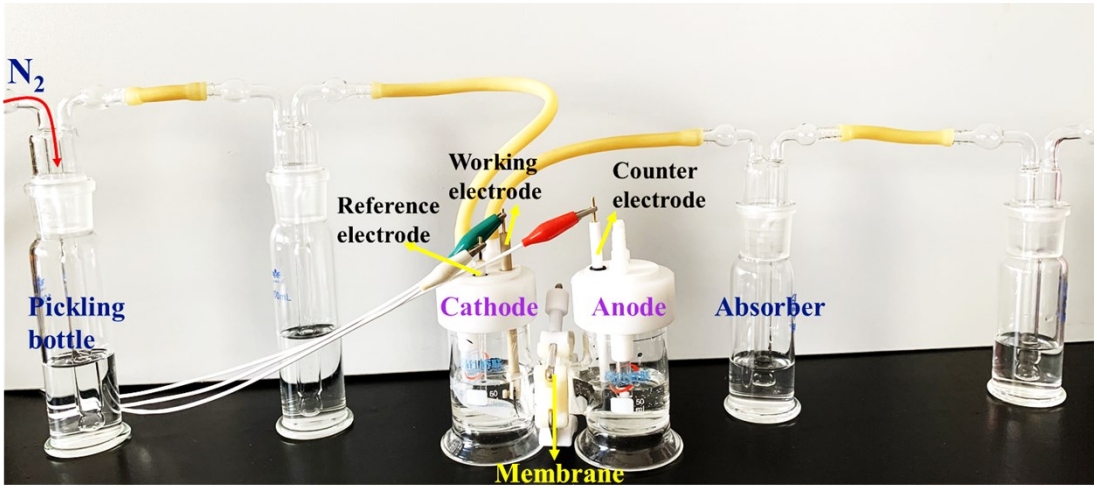

Figure S11. The photograph of H-type reactor with two compartments separated by proton-conductive Nafion 211 membrane and gas absorption purification devices.

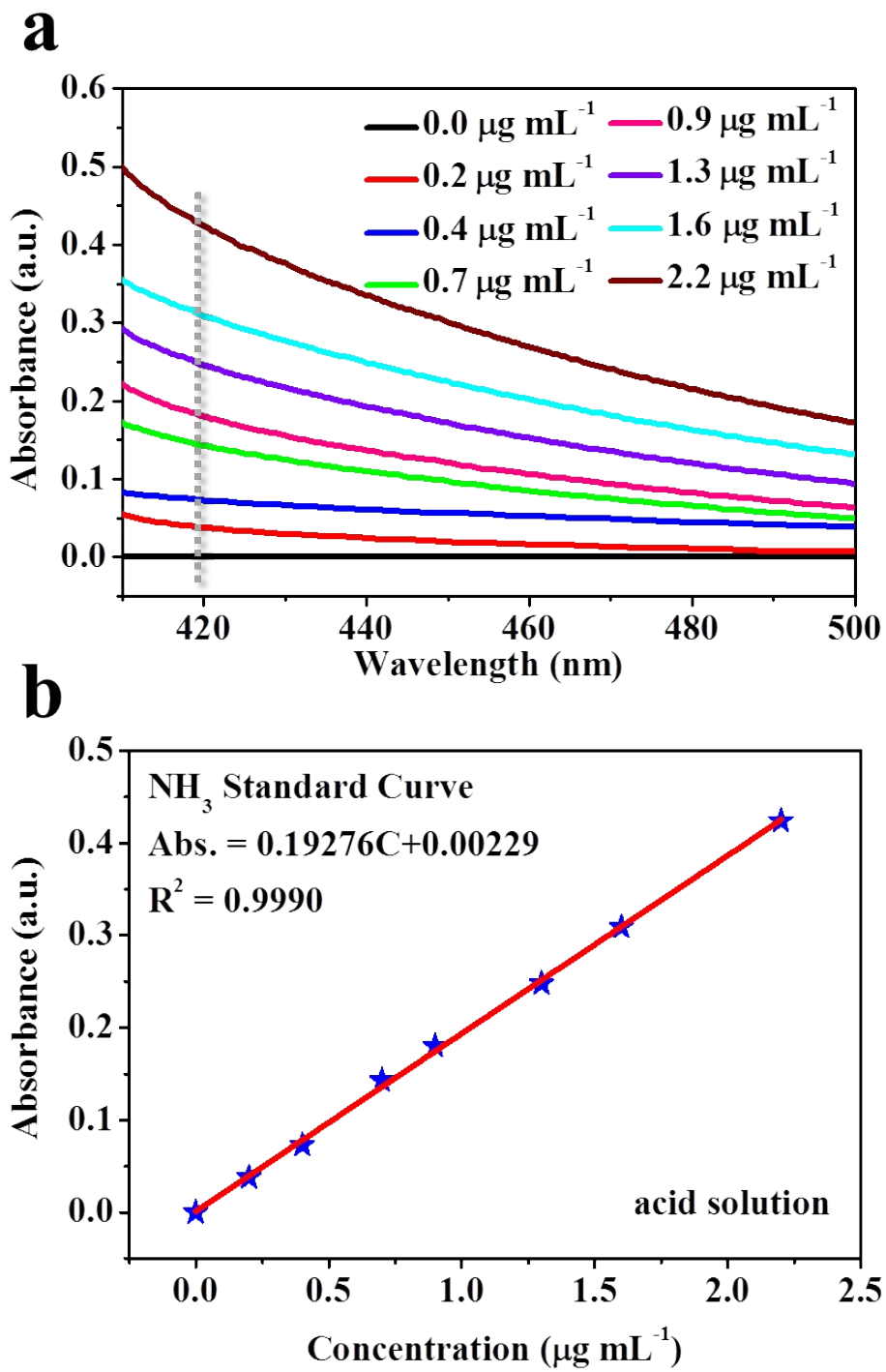

Figure S12. Calibration curve by using Nessler′s reagent in acidic potassium sulfate electrolytes (pH 3.5, 1.0 mol L^{-1} of K^+) and ammonium chloride solutions of known concentration as standards. (a) UV-vis curves of Nessler′s assays after incubated for 30 minutes and (b) calibration curve used for estimation of NH_3 concentration. The absorbance at 420 nm was measured by UV-Vis spectrophotometer, and the fitting curve shows good linear relation of absorbance with NH_3 concentration (y = 0.19276x + 0.00229, R^2=0.9990).

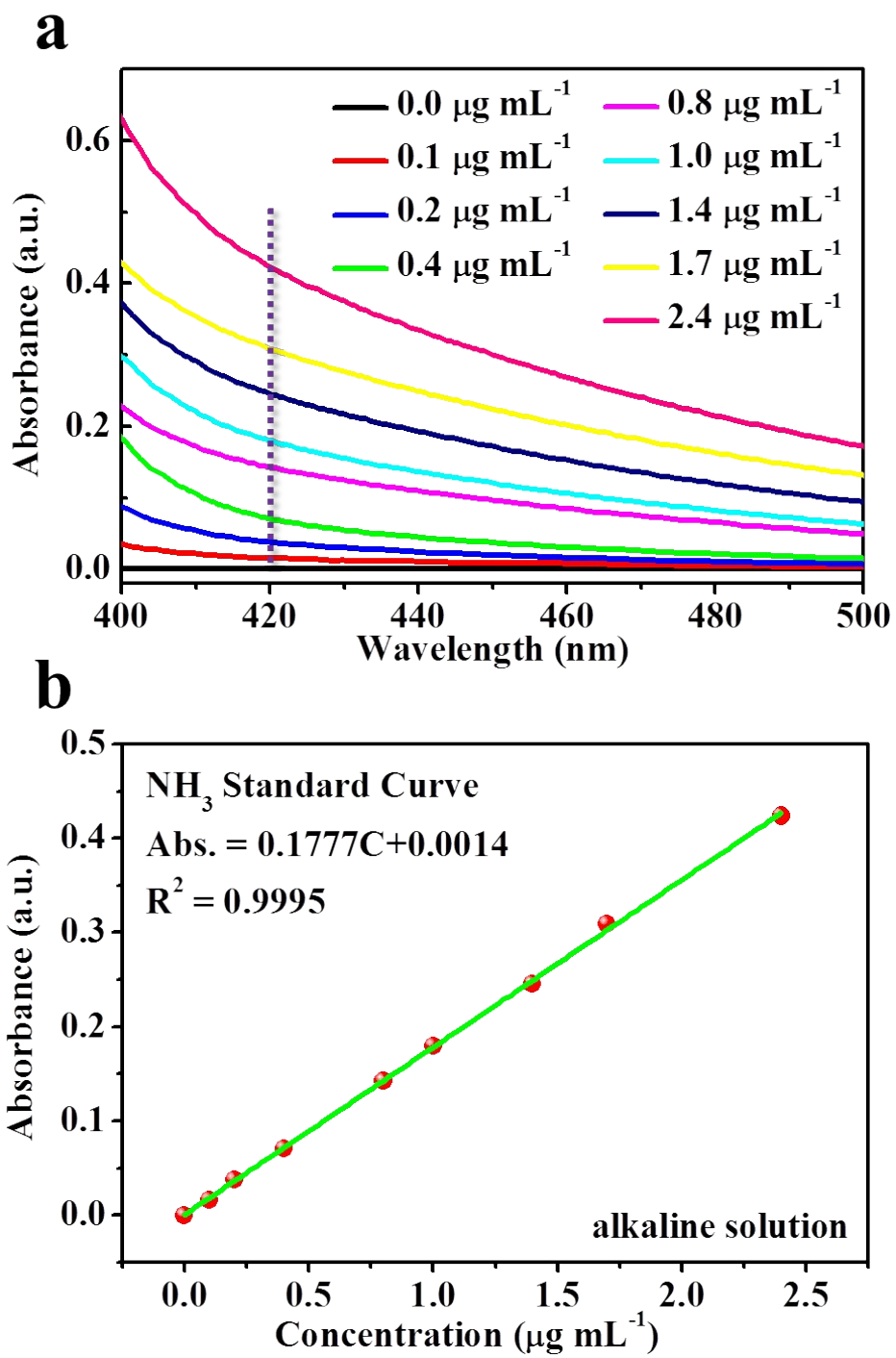

Figure S13. Calibration curve by using Nessler′s reagent in 0.1 M KOH and ammonium chloride solutions of known concentration as standards. (a) UV-vis curves of Nessler′s assays after incubated for 30 minutes and (b) calibration curve used for estimation of NH_3 concentration. The absorbance at 420 nm was measured by UV-Vis spectrophotometer, and the fitting curve shows good linear relation of absorbance with NH_3 concentration ($y = 0.1777x + 0.0014$, R^2=0.9995).

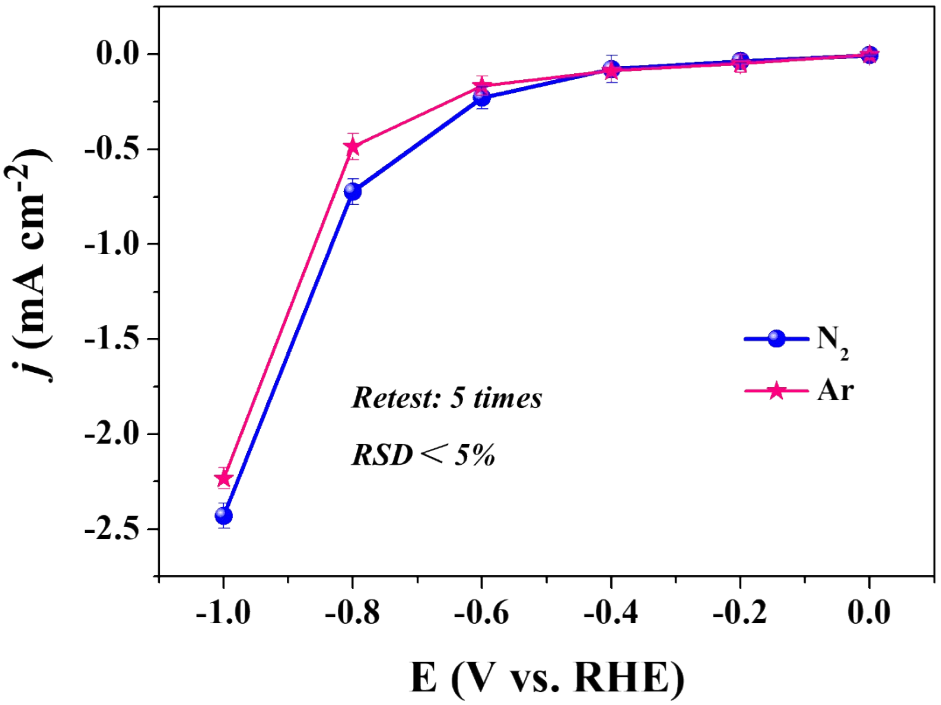

Figure S14. Linear sweep voltammetry (LSV) curves in N_2-saturated (red line) and Ar-saturated (black line) atmospheres between –1 and 0 V vs. RHE with a scan rate of 10.0 mV s^{-1}. Each error bar represents a standard deviation from five measurements.

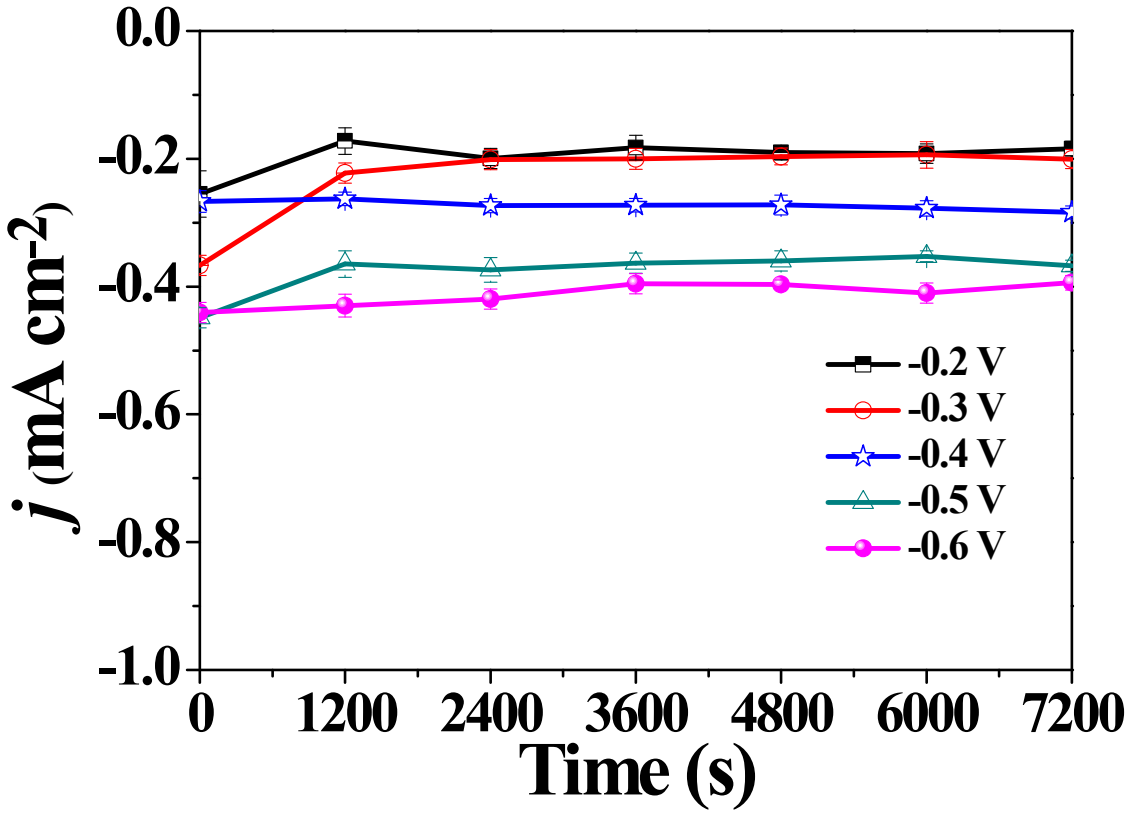

Figure S15. Corresponding chronoamperometric (*j*−t) curves with the error bars

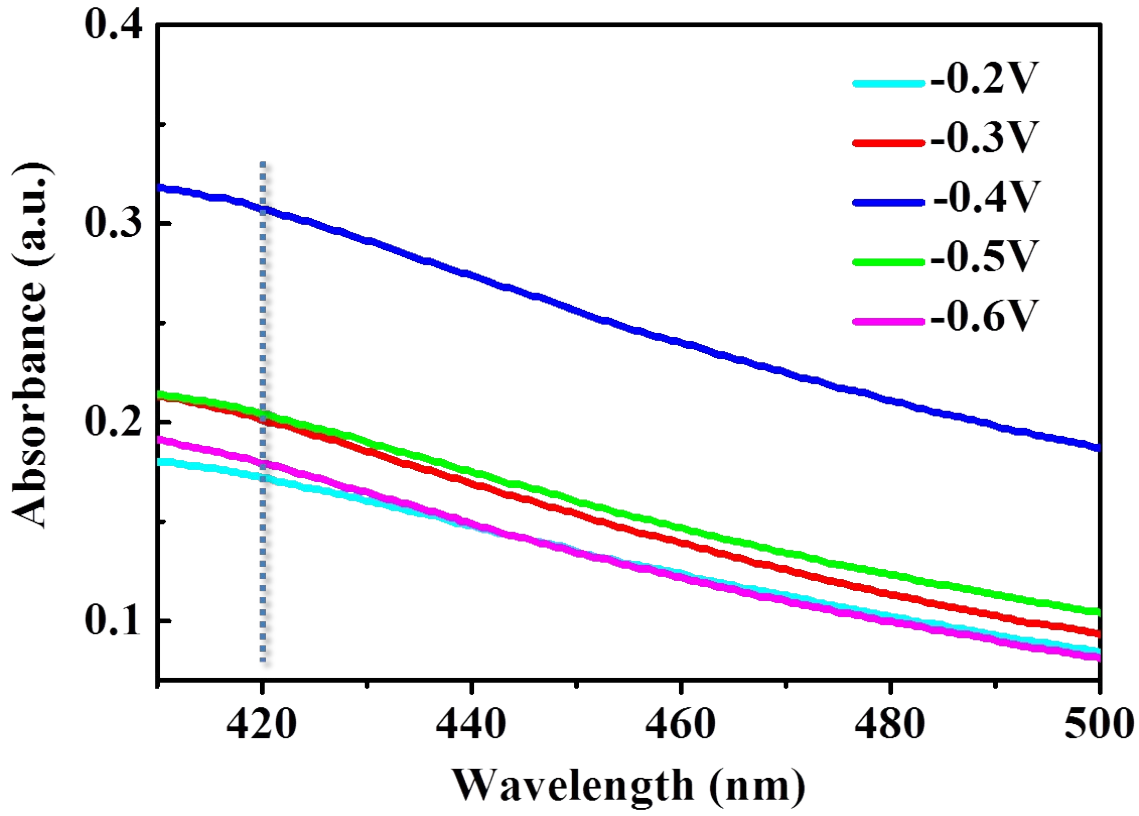

Figure S16. UV-vis curves with Nessler′s reagent after 2 h of electrochemical nitrogen fixation at different voltages (0.2 V–0.6 V) of $Fe_{1.89}Mo_{4.11}O_7/FeS_2$@C (1.6 wt%) catalyst in the acidic potassium sulfate electrolytes (pH 3.5, 1.0 mol L^{-1} of K^+).

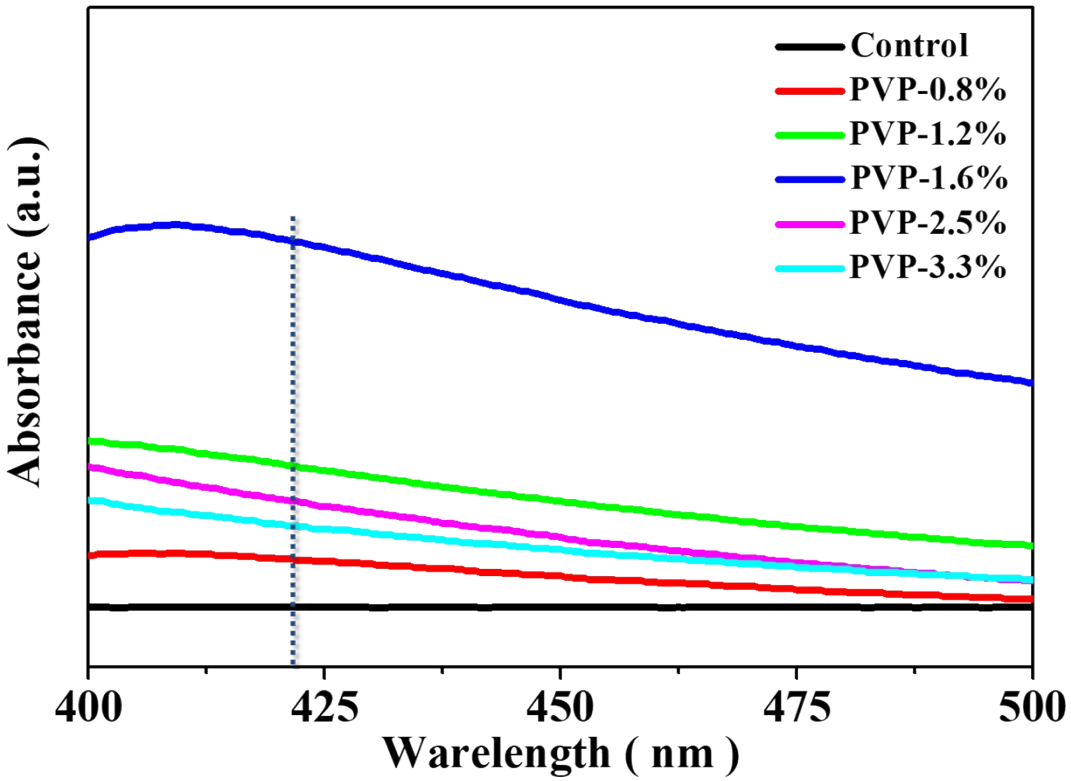

Figure S17. The UV-vis absorption spectra of $Fe_{1.89}Mo_{4.11}O_7/FeS_2$@C catalysts derived from the precursors with different amounts of PVP (0.8, 1.2, 1.6, 2.5 and 3.3 wt%) and Nessler′s reagent after 2 h of the N_2 reduction reaction at −0.4 V vs. RHE in the acidic potassium sulfate electrolytes (pH 3.5, 1.0 mol L^{-1} of K^+).

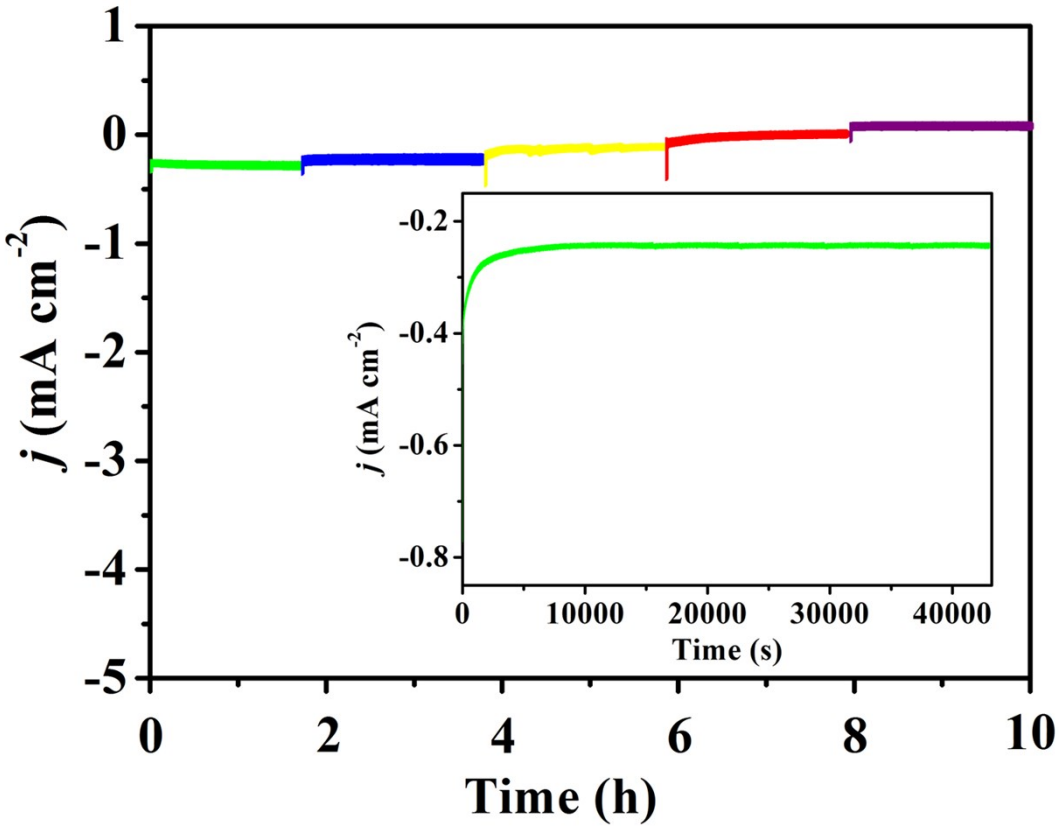

Figure S18. Stability of the chronoamperometry result at −0.4 V vs. RHE using the $Fe_{1.89}Mo_{4.11}O_7/FeS_2$@C (1.6 wt%) for five 2 hour cycles electrolysis, inset: stability of the chronoamperometry result at −0.4 V vs. RHE using the $Fe_{1.89}Mo_{4.11}O_7/FeS_2$@C (1.6 wt%) for consecutive 12 h electrolysis.

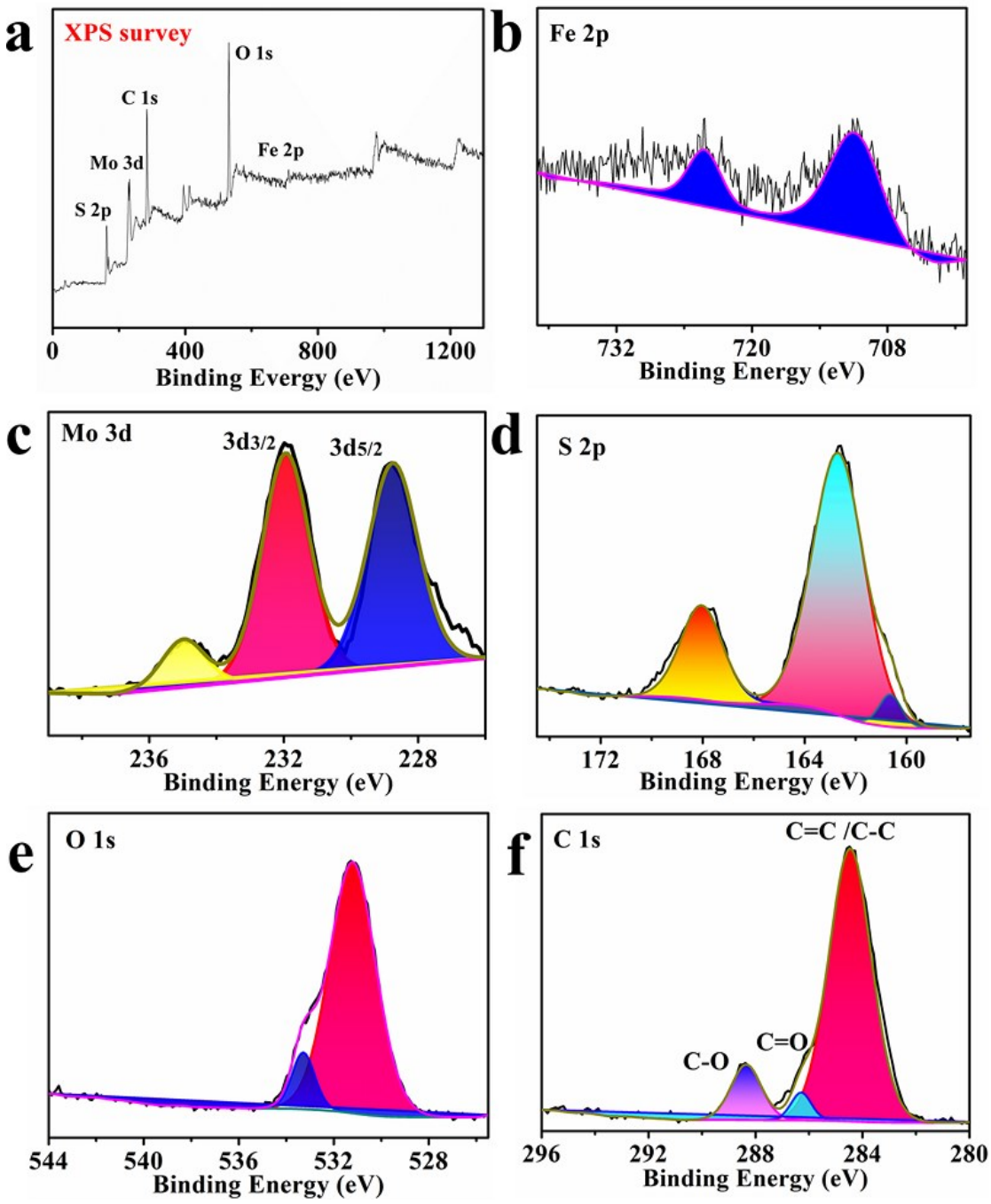

Figure S19. (a) XPS survey spectra and high-resolution scans of (b) Fe 2p (c) Mo 3d (d) S 2p (e) O 1s and (f) C 1s for the $Fe_{1.89}Mo_{4.11}O_7/FeS_2$@C (1.6 wt%) catalyst after 12 h stability test in N_2-saturated solution.

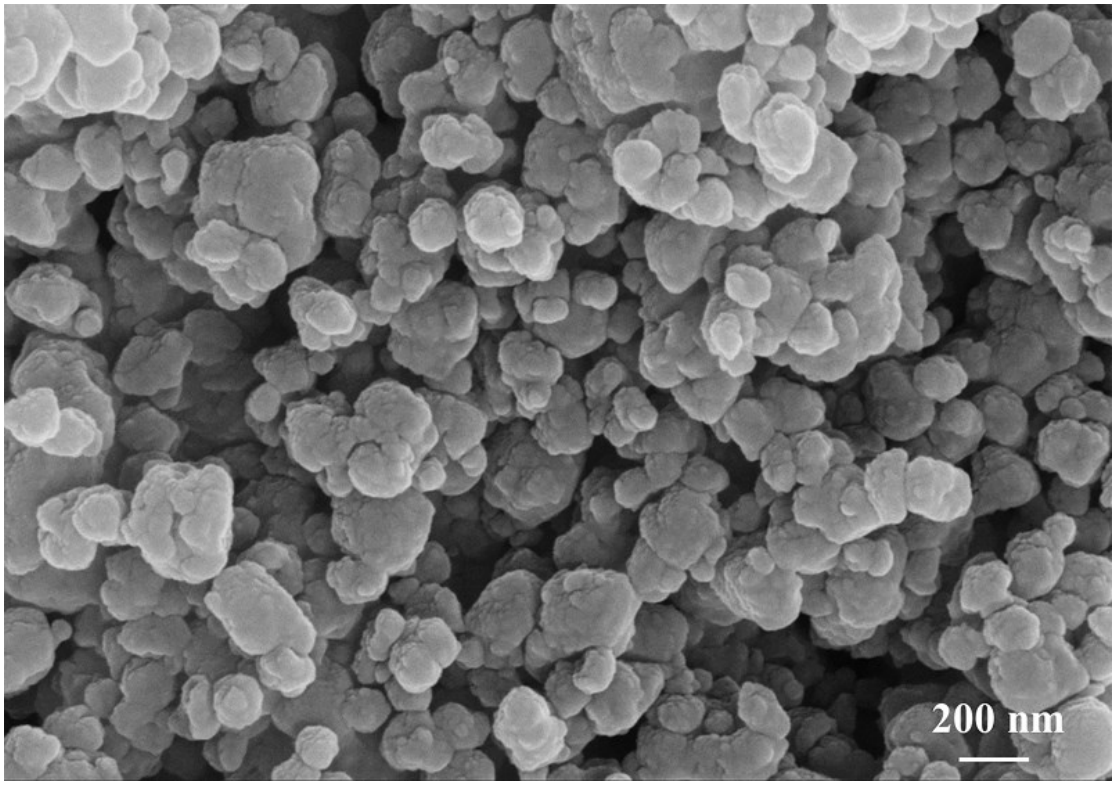

Figure S20. SEM for the $Fe_{1.89}Mo_{4.11}O_7/FeS_2$@C (1.6 wt%) catalyst after 12 h stability test in N_2-saturated solution.

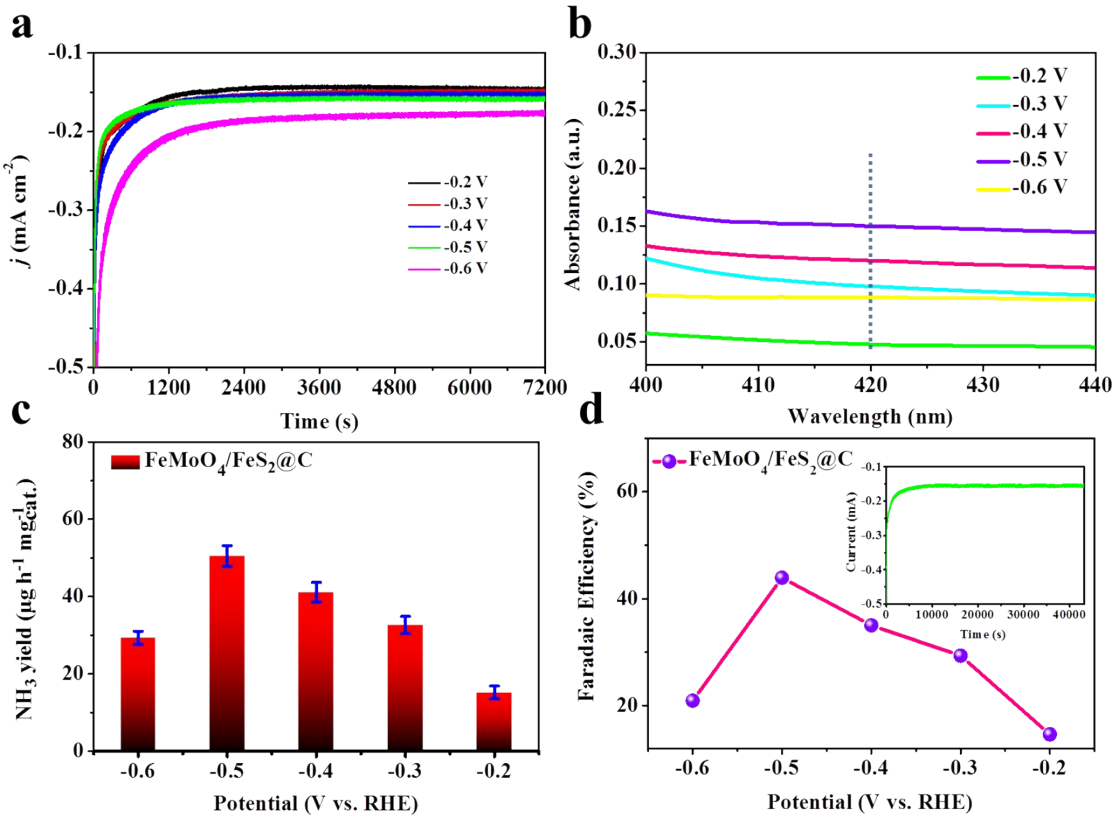

Figure S21. Electrochemical nitrogen fixation on $FeMoO_4/FeS_2$@C catalyst in the acidic potassium sulfate electrolytes (pH 3.5, 1.0 mol L^{-1} of K^+). (a) Time-dependent current density curves of $FeMoO_4/FeS_2$@C under various potentials. (b) UV-vis absorption spectra of the electrolytes stained with the Nessler′s reagent after NRR electrolysis. (c) NH_3 yields under the corresponding potentials (d) Faradaic efficiency under the corresponding potentials, inset: stability of the chronoamperometry result at the potential of −0.5 V vs. RHE using the $FeMoO_4/FeS_2$@C catalyst for 12 h.

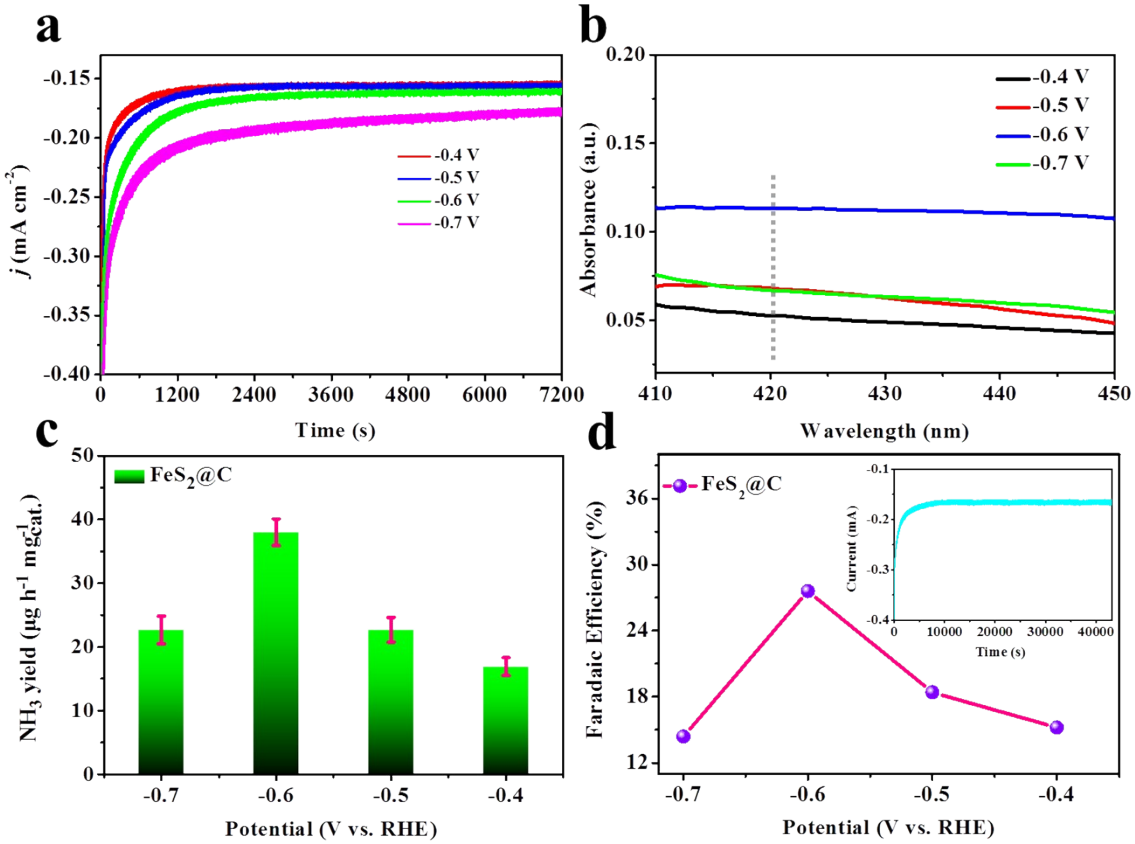

Figure S22. Electrochemical nitrogen fixation on FeS_2@C catalyst in the acidic potassium sulfate electrolytes (pH 3.5, 1.0 mol L^{-1} of K^+). (a) Time-dependent current density curves of FeS_2@C under various potentials. (b) UV-vis absorption spectra of the electrolytes stained with the Nessler′s reagent after NRR electrolysis. (c) NH_3 yields under the corresponding potentials (d) Faradaic efficiency under the corresponding potentials, inset: stability of the chronoamperometry result at the potential of −0.6 V vs. RHE using the FeS_2@C catalyst for 12 h.

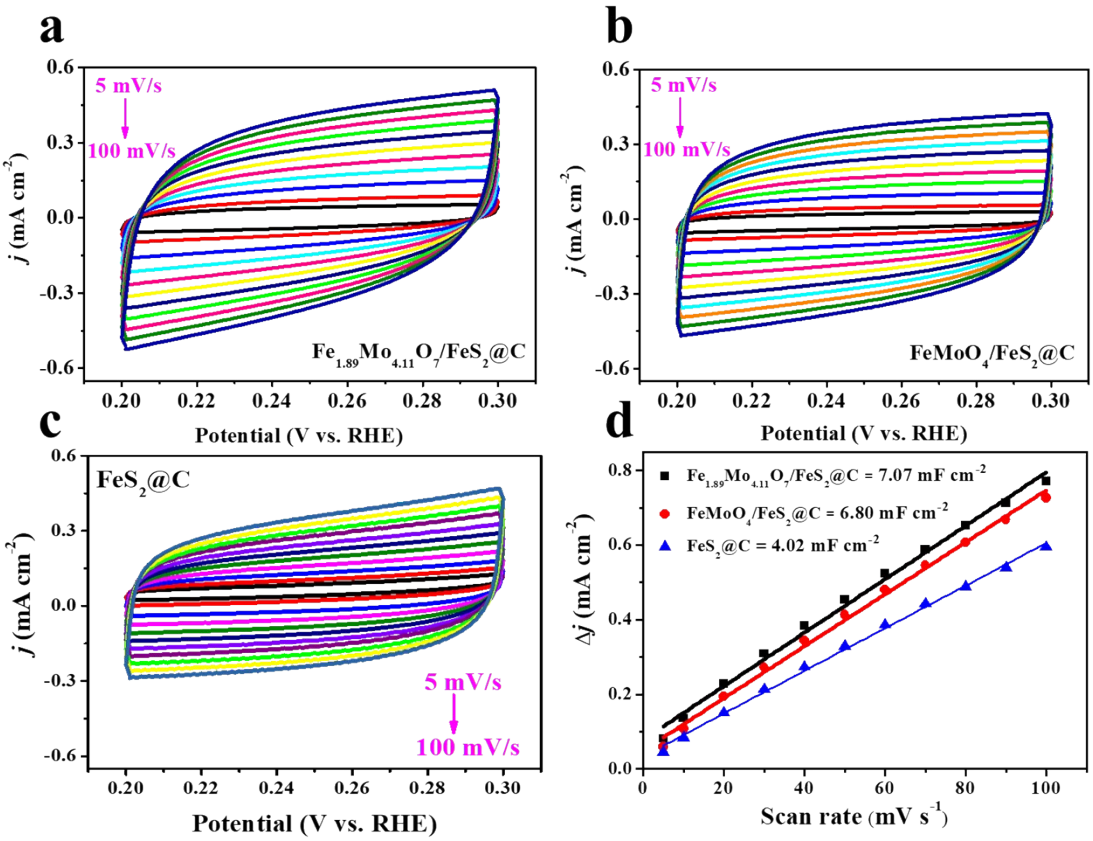

Figure S23. (a-c) Cyclic voltammograms and (d) differences in the charging current density, Δj, plotted against scan rates.

The double layer capacitance (C_{dl}) of the catalytic surface was measured by cyclic voltammetry (CV) in an Ar-saturated acidic potassium sulfate electrolytes (pH 3.5, 1.0 mol L^{-1} of K^{+}) using different scan rates, which was generally used to represent the corresponding electrochemically active surface areas (ECSAs).

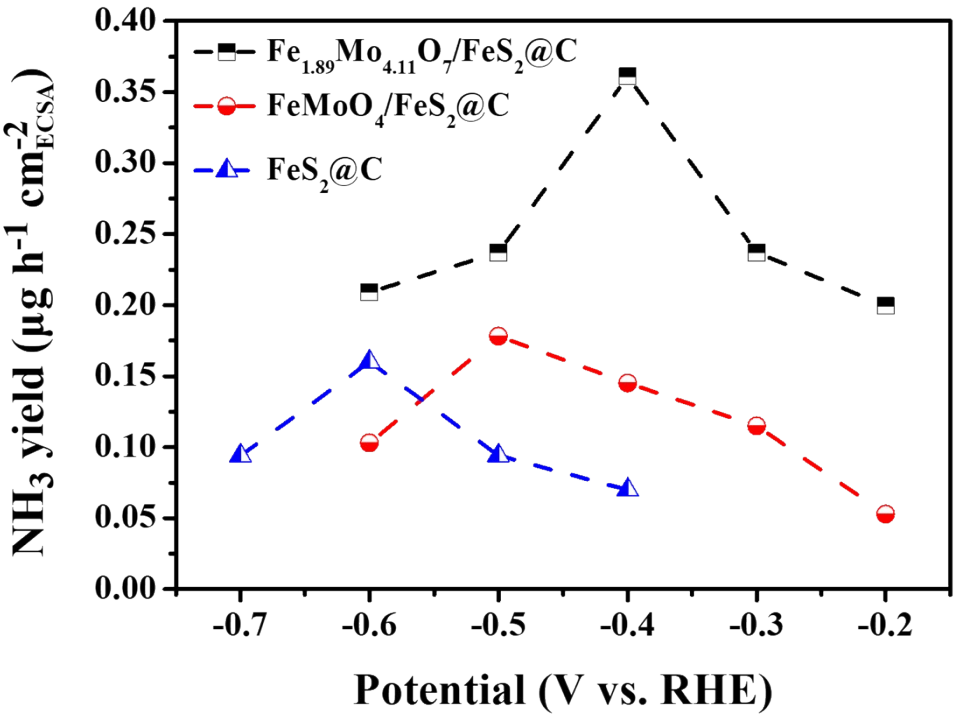

Figure S24. Surface-area-normalized yield rate of NH_3 production at different applied potentials on $Fe_{1.89}Mo_{4.11}O_7/FeS_2$@C (1.6 wt%), $FeMoO_4/FeS_2$@C, and FeS_2@C.

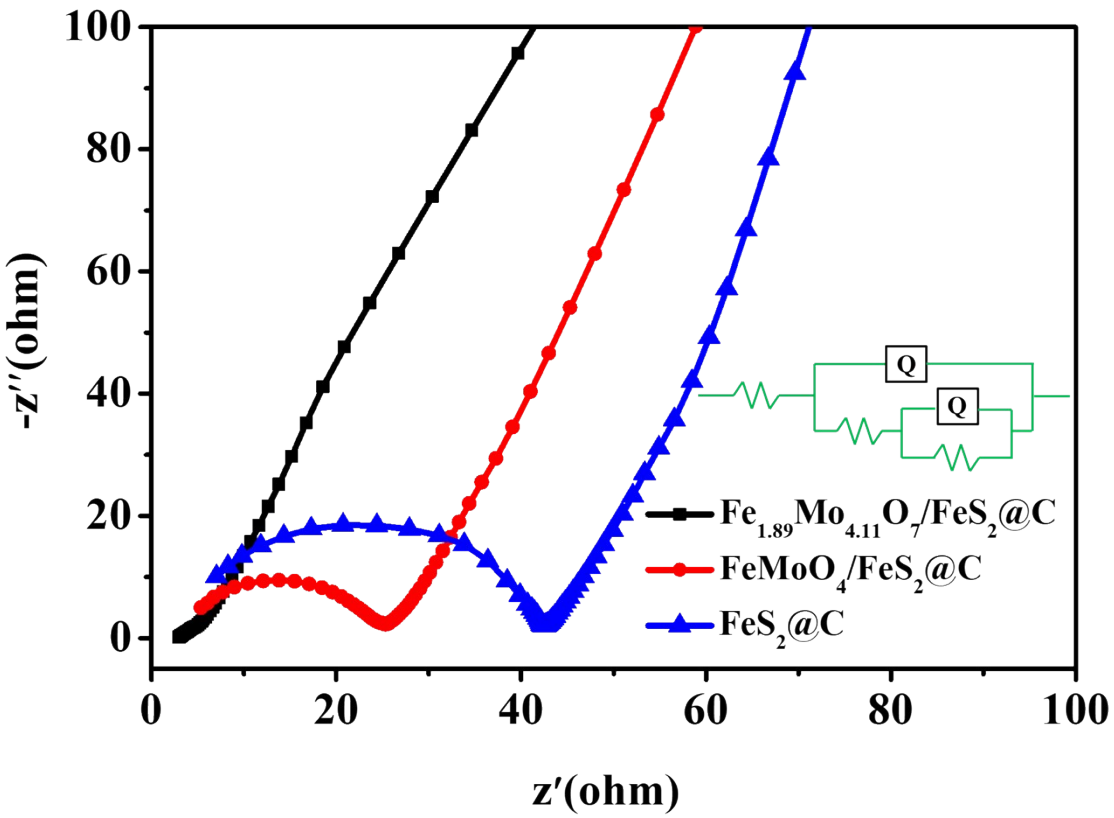

Figure S25. Nyquist plots of electrochemical impedance spectra (EIS) of $Fe_{1.89}Mo_{4.11}O_7/FeS_2@C$ (1.6 wt%), $FeMoO_4/FeS_2@C$, and $FeS_2@C$ in the acidic potassium sulfate electrolytes (pH 3.5, 1.0 mol L^{-1} of K^+). inset is the electrical equivalent circuit model used for data fitting

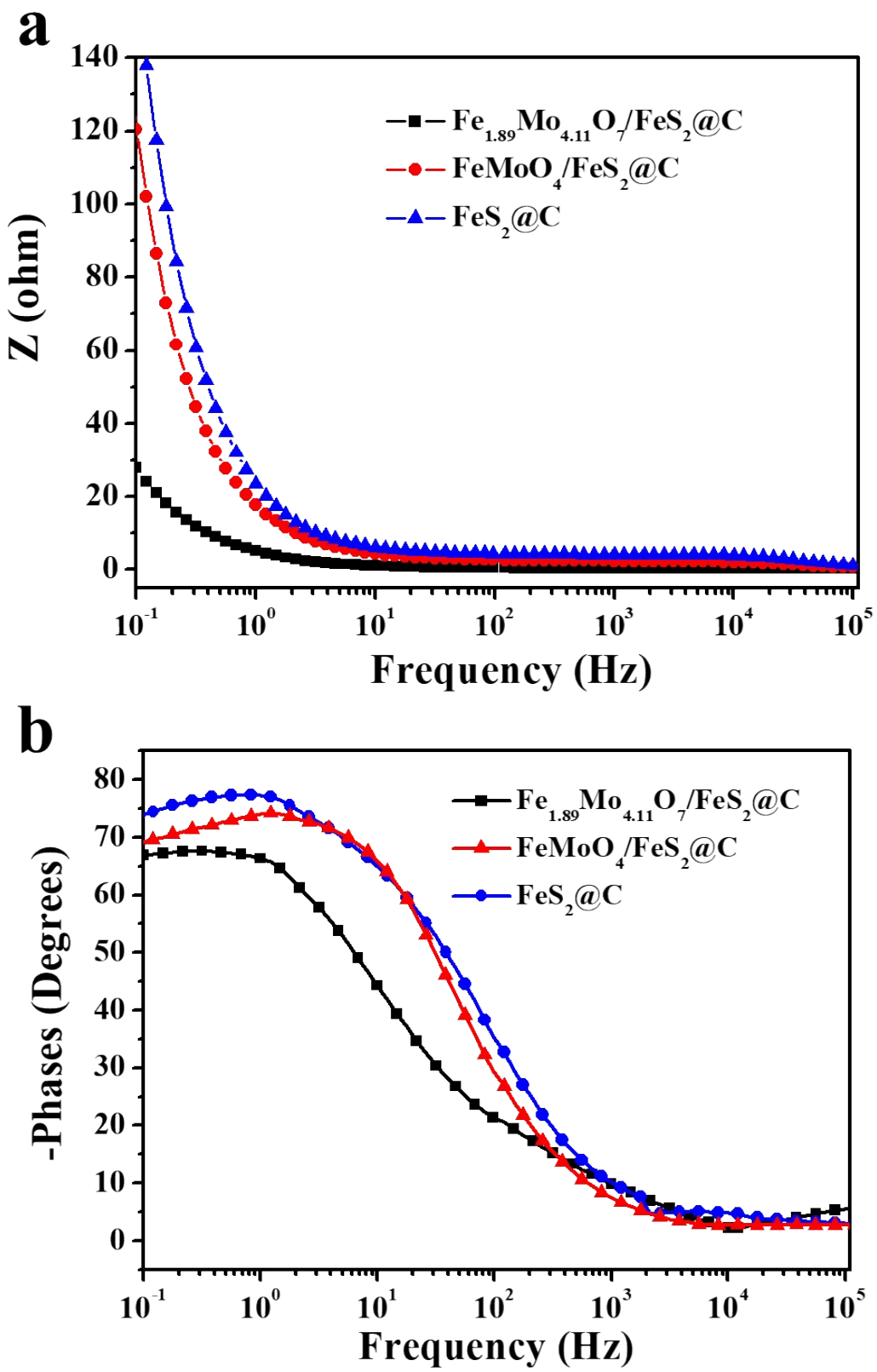

Figure S26. Bode plots of the $Fe_{1.89}Mo_{4.11}O_7/FeS_2$@C (1.6 wt%), $FeMoO_4/FeS_2$@C, and FeS_2@C in the acidic potassium sulfate electrolytes (pH 3.5, 1.0 mol L^{-1} of K^+).

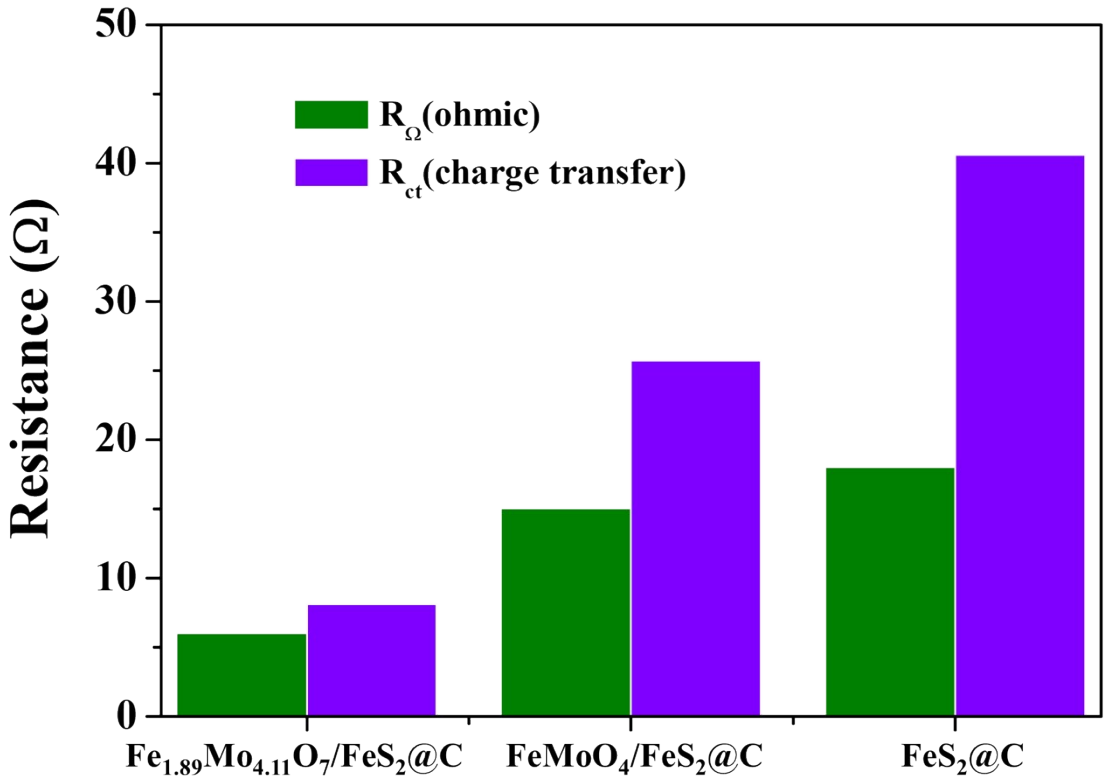

Figure S27. The resistance contributions of $Fe_{1.89}Mo_{4.11}O_7/FeS_2$@C (1.6 wt%), $FeMoO_4/FeS_2$@C, and FeS_2@C on CC electrode.

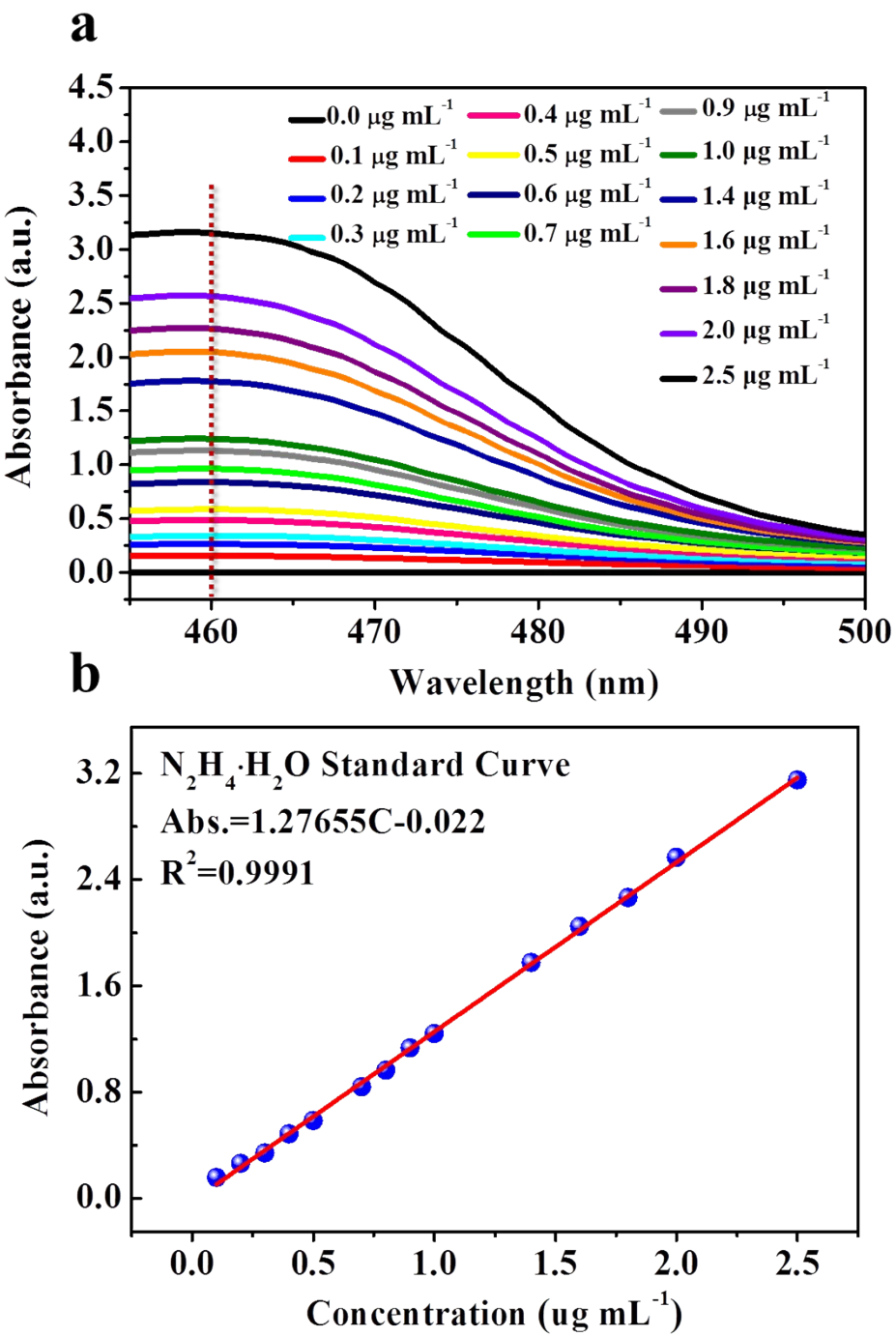

Figure S28. (a) UV-vis curves and (b) the calibration curve for the colorimetric $N_2H_4 \cdot H_2O$ assay using the Watt and Chrisp method.

The absorbance at 460 nm was measured by UV-Vis spectrophotometer, and the fitting curve shows good linear relation of absorbance with $N_2H_4 \cdot H_2O$ concentration ($y = 0.1.27655x - 0.022$, $R^2=0.9991$). The value for acidic potassium sulfate electrolytes (pH 3.5, 1.0 mol l^{-1} of K^+) was subtracted from all of the data as the background.

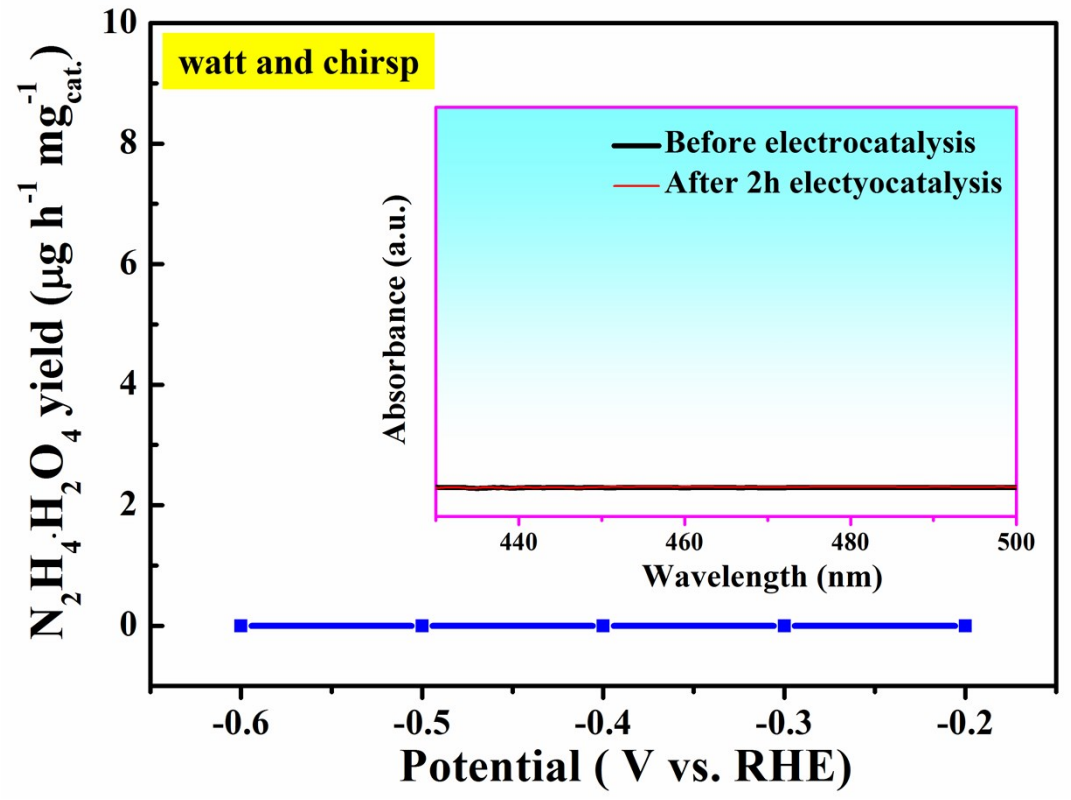

Figure S29. The yield rate of $N_2H_4{\cdot}H_2O$ formation and corresponding UV-vis absorption spectra of the acidic potassium sulfate electrolytes (pH 3.5, 1.0 mol L^{-1} of K^+) electrolyte stained with a para-dimethylamino-benzaldehyde indicator at each given potential vs. RHE for 2 h.

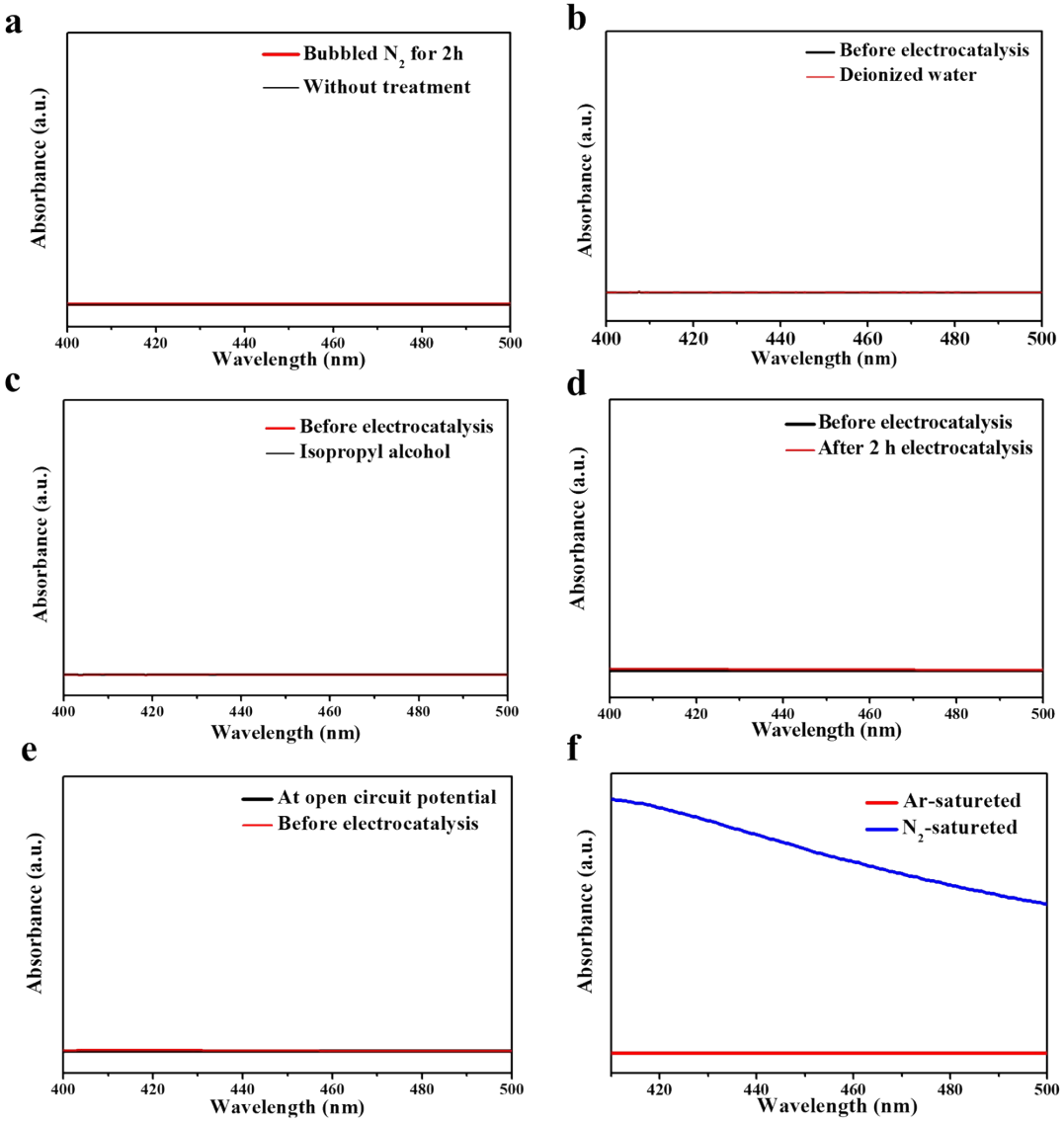

Figure S30. The UV-vis absorption spectra of (a) the electrolyte before and after N_2 bubbling for 2 h. (b) the deionized water and (c) the isopropyl alcohol after incubated with NH_3 color agent under ambient conditions. (d) a carbon cloth electrode with Nafion mixed solution dispersed before and after the electrocatalysis at −0.4 V vs. RHE 2 h. (e) The same condition with the electrochemical NRR procedure at open circuit potential for 2 h. (f) $Fe_{1.89}Mo_{4.11}O_7/FeS_2$@C (1.6wt%) along with N_2 or Ar bubbling after electrocatalysis at −0.4 V vs. RHE for 2 h, respectively.

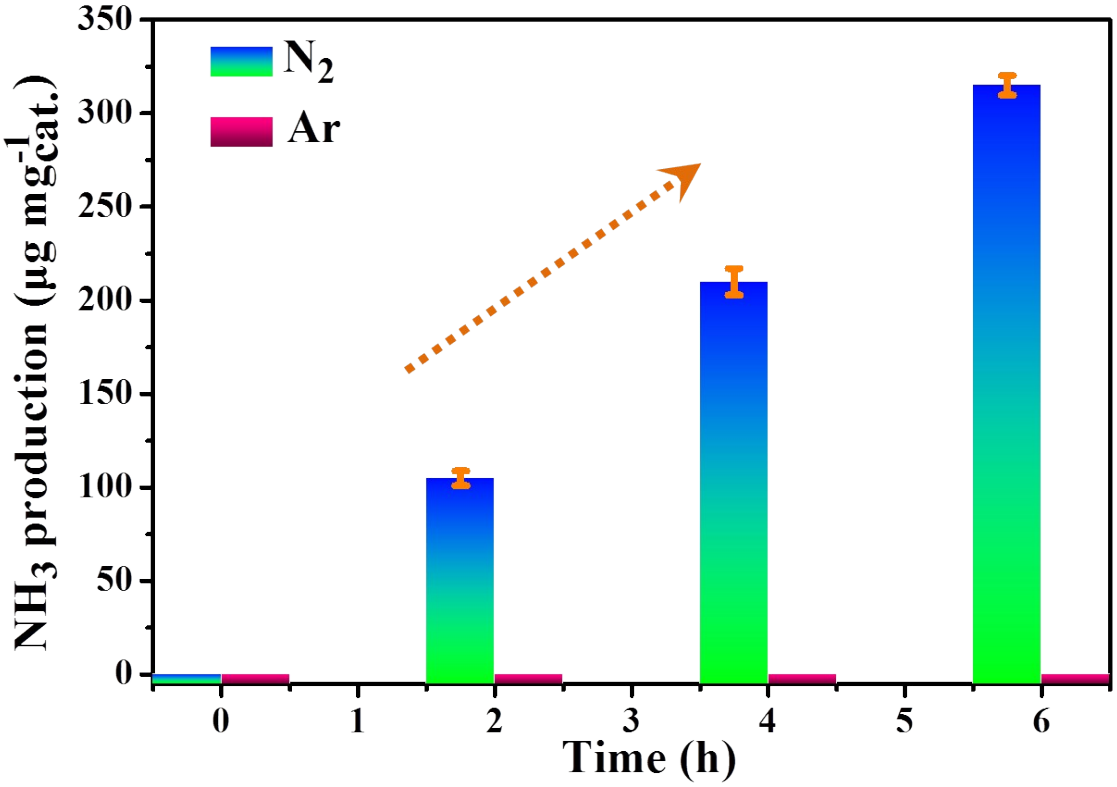

Figure S31. NH_3 yields of $Fe_{1.89}Mo_{4.11}O_7/FeS_2$@C (1.6 wt%) after electrolysis at –0.4 V vs. RHE for 6 h consecutive electrolysis bubbled with N_2 or Ar, respectively.

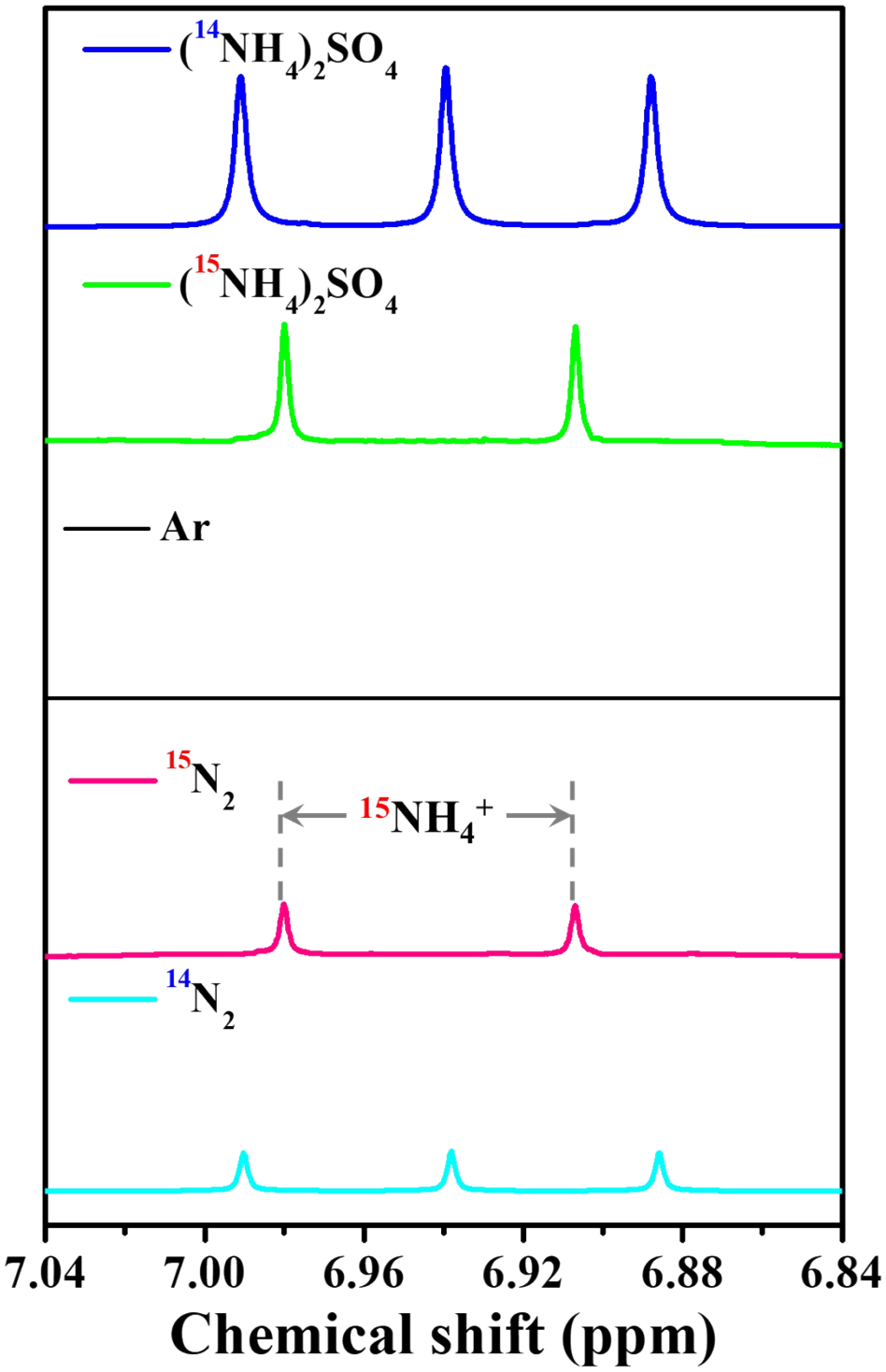

Figure S32. ^{1}H NMR analysis of the electrolyte fed by $^{14}N_2$ and $^{15}N_2$ after the electrolytic reaction.

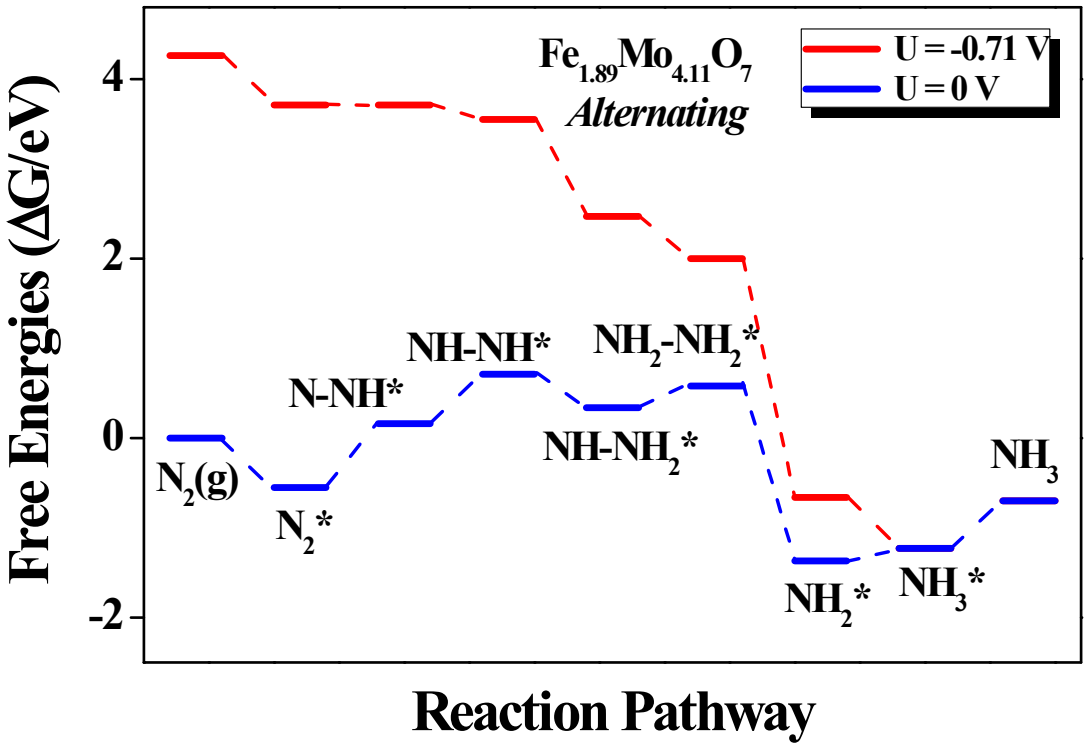

Figure S33. Gibbs free energies, in eV at RTP, for the alternating pathway on $Fe_{1.89}Mo_{4.11}O_7$ (002), when there is no applied bias (U = 0 V) and pH = 0. Note: an asterisk (*) denoted as the adsorption site.

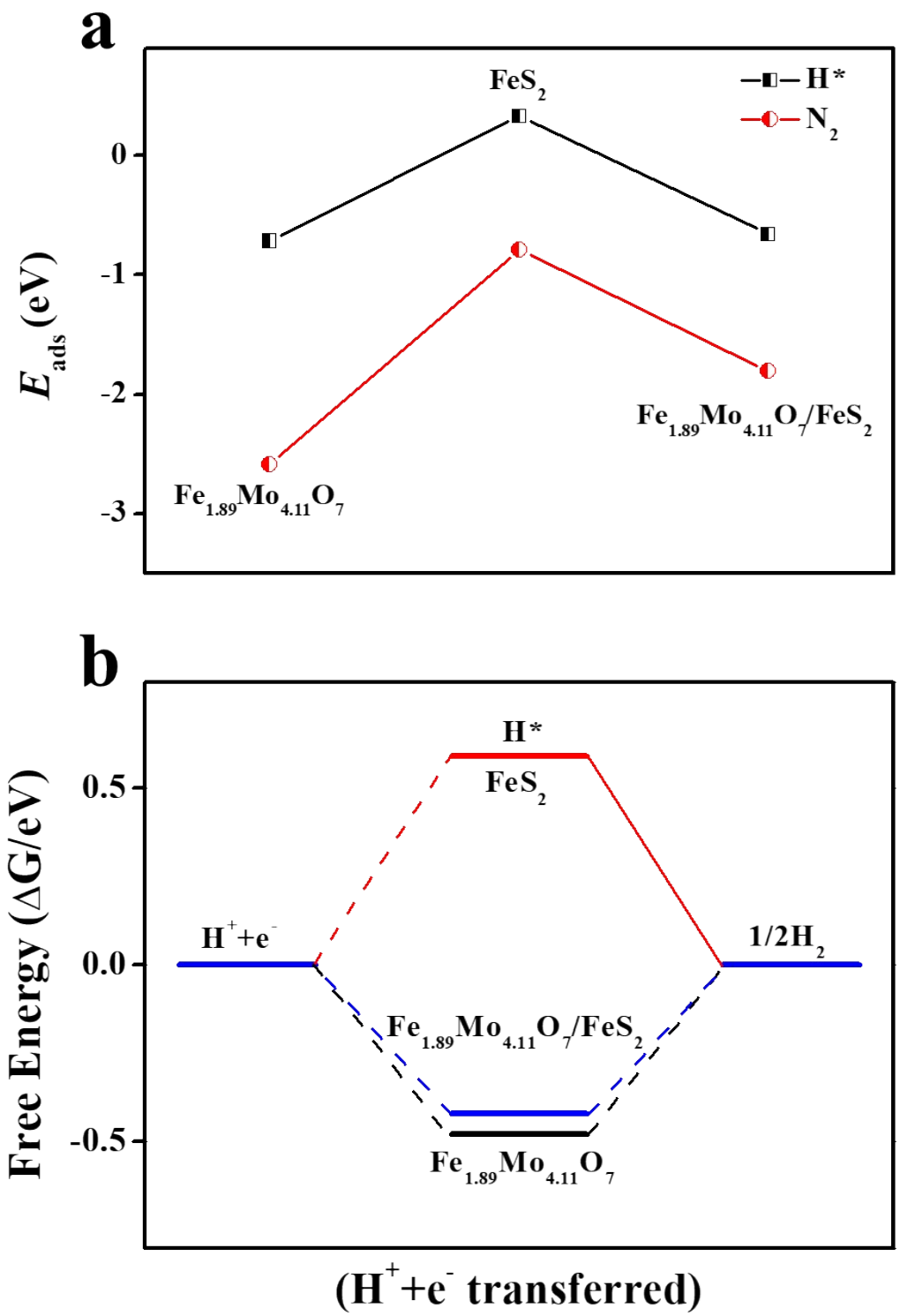

Figure S34. (a) The computed adsorption energies of H* and N_2 on different models, and (b) the Δ*G* diagram of the HER on these catalysts.

Table S1. Summary of part of representative NRR electrocatalysts reported in recent years and their catalytic performance

Catalysts	Electrolyte	FE (%)	Yield (NH_3)	Applied Potential vs RHE	Ref.	year
$Fe_{1.89}Mo_{4.11}O_7/FeS_2$@C	pH 3.5, 1.0 mol L^{-1} of K^+	54.7	105.3 μg h^{-1} $mg_{cat.}^{-1}$	–0.4	**This work**	**2020**
	0.1 M KOH	53.6	86.3 μg h^{-1} $mg_{cat.}^{-1}$	–0.4		
$FeMoO_4/FeS_2$@C	pH 3.5, 1.0 mol L^{-1} of K^+	43.9	51.0 μg h^{-1} $mg_{cat.}^{-1}$	–0.5		
FeS_2@C	pH 3.5, 1.0 mol L^{-1} of K^+	27.6	38.6 μg h^{-1} $mg_{cat.}^{-1}$	–0.6		
Fe_2O_3 nanorods	0.1 M Na_2SO_4	0.94	15.9 μg h^{-1} cm^{-2}	–0.8	16	2018
Fe/Fe_3O_4	0.1 M PBS	8.29	0.19 μg h^{-1} cm^{-2}	–0.3	17	2018
Fe_3O_4/Ti	0.1 M Na_2SO_4	2.6	5.6×10^{-11} mol s^{-1} cm^{-2}	–0.4	18	2018
γ-Fe_2O_3-NC/CF[a]	0.1 M HCl	12.28	11.7×10^{-10} mol s^{-1} cm^{-2}	–0.1	19	2019
Au-Fe_3O_4	0.1 M KOH	10.54	21.42 μg h^{-1} $mg_{cat.}^{-1}$	–0.2	20	2019
FeS_2/CFP[b]	0.25 M $LiClO_4$	14.14	0.096 μg min^{-1}	–0.6	21	2019
(110)-oriented Mo	0.01 M H_2SO_4	0.72	3.09×10^{-11} mol s^{-1} cm^{-2}	–0.49	22	2017
MoS_2/CC	0.1 M Na_2SO_4	1.17	4.94 μg h^{-1} cm^{-2}	–0.5	23	2018
Mo_2C/C	0.5 M Li_2SO_4	7.8	3.78 μg h^{-1} $mg_{cat.}^{-1}$	–0.3	24	2018
SA-Mo/NPC[c]	0.1 M KOH	14.6 ±1.6	34.0 ± 3.6 μg h^{-1} $mg_{cat.}^{-1}$	–0.25	25	2019
MoS_2/BCCF[d]	0.1 M Li_2SO_4	9.81	43.4 μg h^{-1} mg^{-1} MoS_2	– 0.2	26	2019
Ru/MoS_2	10 Mm HCl	17.6	1.14×10^{-10} mol s^{-1} cm^{-2}	–0.2	27	2019
Mo_3Fe_3C	0.1 M Li_2SO_4	27.0	72.5 μmol h^{-1} $g_{cat.}^{-1}$	–0.05	28	2019
FeS@MoS_2/CFC[e]	0.1 M Na_2SO_4	2.96	8.45 μg h^{-1} cm^{-2}	–0.5	29	2019
MoFe-PC	0.1 M HC	16.83	34.23 μg h^{-1} $mg_{cat.}^{-1}$	–0.5	30	2020

Ru SAs/N-C[f]	0.05 M H_2SO_4	29.6	120.9 μg_{NH3} $mg_{cat.}^{-1}$ h^{-1}	–0.2	31	2018
Ru/CFP	0.01 M HCl	5.4	0.20 μg h^{-1} cm^{-2}	0.01	32	2018
Ru/NC	0.1 M HCl	~8	4.6 μg h^{-1} $mg_{cat.}^{-1}$	–0.21	33	2018
Ru/ZrO_2/NC	0.1 M HCl	15	3 μg h^{-1} $mg_{cat.}^{-1}$	–0.21		2018
RuPt/C	1.0 M KOH	13.2	18.36 μg h^{-1} cm^{-2}	1.23	34	2018
Au/TiO_2	0.1 M HCl	8.11	21.4 μg h^{-1} $mg_{cat.}^{-1}$	–0.2	35	2017
Au thin film	0.1 M KOH	0.12	0.235 μg h^{-1} cm^{-2}	– 0.5	36	2018
Au HNC[g]	0.5 M $LiClO_4$	30.22	3.98 μg h^{-1} cm^{-2}	–0.5	37	2018
Au flowers	0.1 M HCl	6.05	10.23 μg h^{-1} cm^{-2}	–0.2	38	2018
Au_1/C_3N_4	0.005 M H_2SO_4	11.1	1.961 μg h^{-1} $mg_{cat.}^{-1}$	–0.1	39	2018
Au_x/Ni	0.05 M H_2SO_4	67.8	7.4 μg h^{-1} $mg_{cat.}^{-1}$	–0.14	40	2019
Pd/C	0.1 M PBS	8.2	1.35 μg h^{-1} $mg_{cat.}^{-1}$	0.1	41	2018
Rh NNs[h]	0.1 M KOH	0.217	7.45 mg h^{-1} cm^{-2}	–0.2	42	2018

Notes:

a: γ-Fe_2O_3-NC/CF, N-doped carbon-coated gamma-Fe_2O_3 nanoparticles supported on carbon fabric

b: FeS_2/CFP, iron pyrite nanocrystals grown on carbon fiber paper

c: SA-Mo/NPC, single Mo atoms anchored on N-doped porous carbon

d: MoS_2/BCCF, MoS_2 nanosheets coated commercial bacterial cellulose converted carbon fibers

e: FeS@MoS_2/CFC, a carbon fiber cloth (CFC) covered with FeS dotted MoS_2 nanosheets

f: Ru SAs/N-C, Ru single atoms distributed on nitrogen-doped carbon

g: Au HNC, hollow gold nanocages

h: Rh NNs, Rh nanosheet nanoassemblies

Table S2. The free-energy change (ΔG) for N_2 hydrogenation on $Fe_{1.89}Mo_{4.11}O_7$ (002)

Site	Elementary Step	ΔG/eV
Fe	$N_2^* + H^+ + e^- \rightarrow *N–NH$	1.14
Mo	$N_2^* + H^+ + e^- \rightarrow *N–NH$	0.71

Reference

1 R. Canioni, C. Roch-Marchal, F. Secheresse, P. Horcajada, C. Serre, M. Hardi-Dan, G. Ferey, J. M. Greneche, F. Lefebvre, J. S. Chang, Y. K. Hwang, O. Lebedev, S. Turner and G. V. Tendeloo, *J. Mater. Chem.*, 2011, **21**, 1226–1233.

2 S. Suarez and D. Paterno, *J. Power Sources,* 2016, **331**, 544–552.

3 Y. Wang, X. Q. Cui, J.-X. Zhao, G.-R. Jia, L. Gu, Q.-H. Zhang, L.-K. Meng, Z. Shi, L.-R. Zheng, C.-Y. Wang, Z.-W. Zhang and W.-T. Zheng, *ACS Catal*., 2019, **9**, 336−344.

4 C.-J. Zhao, S.-B. Zhang, M.-M. Han, X. Zhang, Y.-Y. Liu, W.-Y. Li, C. Chen, G.-Z. Wang, H.-M. Zhang and H.-J. Zhao, *ACS Energy Lett.*, 2019, **4**, 377−383.

5 G. Kresse and J. Furthmüller, *Phys. Rev. B*, 1996, **54**, 11169–11186.

6 G. Kresse and J. Furthmüller, *Comput. Mater. Sci.*, 1996, **6**, 15–50.

7 J. P. Perdew, K. Burkea and M. Ernzerhof, *Phys. Rev. Lett.*, 1996, **77**, 3865–3868.

8 P. E. Blöchl, *Phys. Rev. B*, 1994, **50**, 17953–17979.

9 T. B. Van, M. Torrent and X. Gonze, *Phys. Rev. B*, 2016, **93**, 144304.

10 J. Rossmeisl, A. Logadottir and J. K. Nørskov, *Chem. Phys.*, 2005, **319**, 178–184.

11 A. A. Peterson, F. Abild–Pedersen, F. Studt, J. Rossmeisl and J. K. Nørskov, *Energy Environ. Sci.*, 2010, **3**, 1311–1315.

12 J. K. Nørskov, J. Rossmeisl, A. Logadottir and L. Lindqvist, *J. Phys. Chem. B*, 2004, **108**, 17886−17892.

13 D. H. Lim and J. Wilcox, *J. Phys. Chem. C.*, 2012, **116**, 3653−3660.

14 Y. Wang, H. Yuan, Y.-F. Li and Z.-F. Chen, *Nanoscale* , 2015, **7**, 11633–11641.

15 S. Kattel, P. Atanassov and B. Kiefer, *J. Phys. Chem. C*, 2012, **116**, 17378–17383.

16 X.-J. Xiang, Z. Wang, X.-F. Shi, M.-K. Fan and X.-P. Sun, *ChemCatChem*, 2018, **10**, 4530–4535.

17 L. Hu, A. Khaniya, J. Wang, G. Chen, W. E. Kaden and X.-F. Feng, *ACS Catal.*, 2018, **8**, 9312–9319.

18 Q. Liu, X.-X. Zhang, B. Zhang, Y.-L. Luo, G.-W. Cui, F.-Y. Xie and X.-P. Sun, *Nanoscale*, 2018, **10**, 14386–14389.

19 Y. Li, Y. Kong, Y. Hou, B. Yang, Z.-J. Li, L.-C. Lei and Z.-H. Wen, *ACS Sustainable Chem. Eng.*, 2019, **7**, 8853–8859.

20 J. Zhang, Y.-J. Ji, P.-T. Wang, Q. Shao, Y.-Y. Li and X.-Q. Huang, *Adv. Funct. Mater.*, 2019, **30**, 1906579.

21 C.-C. Chang, S.-R. Li, H.-L. Chou, Y.-C. Lee, S. Patil, Y.-S. Lin, C.-C. Chang, Y.-J. Chang and D.-Y. Wang, *Small*, 2019, **15**, 1904723.

22 D.-S. Yang, T. Chen and Z.-J. Wang, *J. Mater. Chem. A.*, 2017, **5**, 18967–18971.

23 L. Zhang, X.-Q. Ji, X. Ren, Y.-J. Ma, X.-F. Shi, Z.-Q. Tian, A.-M. Asiri, L. Chen, B. Tang and X.-P. Sun, *Adv. Mater.*, 2018, **30**, 1800191.

24 H. Cheng, L.-X. Ding, G.-F. Chen, L.-L. Zhang, J. Xue and H.-H. Wang, *Adv. Mater.*, 2018, **30**, 1803694.

25 L.-L. Han, X.-J. Liu, J.-P. Chen, R.-Q. Lin, H.-X. Liu, F. Lü, S. Bak, Z.-X. Liang, S.-Z. Zhao, E. Stavitski, J. Luo, R.-R. Adzic and H.-L. Xin, Angew. *Chem. Int. Ed.*, 2019, **58**, 2321–2325.

26 Y.-Y. Liu, M.-M. Han, Q.-Z. Xiong, S.-B. Zhang, C.-J. Zhao, W.-B. Gong, G.-Z. Wang, H.-M. Zhang and H.-J. Zhao, *Adv. Energy Mater.*, 2019, **9**, 1803935.

27 B. H. R. Suryanto, D.-B. Wang, L. M. Azofra, M. Harb, L. Cavallo, R. Jalili, D. R. G. Mitchell, M. Chatti and D. R. MacFarlane, *ACS Energy Lett.*, 2019, **4**, 430–435.

28 B.-H. Qin, Y.-H. Li, Q. Zhang, G.-X. Yang, H. Liang and F. Peng, *Nano energy*, 2020, **68**, 104374.

29 Y.-X. Guo, Z.-Y. Yao, B. J. J. Timmer, X. Sheng, L.-Z. Fan, Y.-Y. Li, F.-G. Zhang and L.-C. Sun, *Nano Energy*, 2019, **62**, 282–288.

30 S.-L. Chen, H. Jang, J. Wang, Q. Qin, X. Liu and J. Cho, *J. Mater. Chem. A*, 2020, **8**, 2099–2104.

31 Z.-G. Geng, Y. Liu, X.-D. Kong, P. Li, K. Li, Z.-Y. Liu, J.-J. Du, M. Shu, R. Si and J. Zeng, *Adv. Mater.*, 2018, **30**, 1803.

32 D.-B. Wang, L. M. Azofra, M. Harb, L. Cavallo, X.-Y. Zhang, B. H. R. Suryanto and D. R. MacFarlane, *ChemSusChem*, 2018, **11**, 3416–3422.

33 H.-C. Tao, C. Choi, L.-X. Ding, Z. Jiang, Z.-S. Han, M.-W. Jia, Q. Fan, Y.-N. Gao, H.-H. Wang, A. W. Robertson, S. Hong, Y.-S. Jung, S.-Z. Liu and Z.-Y. Sun, *Chem.*, 2019, **5**, 204–214.

34 R. Manjunatha and A. Schechter, *Electrochem. Commun.*, 2018, **90**, 96–100.

35 M.-M. Shi, D. Bao, B.-R. Wulan, Y.-H. Li, Y.-F. Zhang, J.-M. Yan and Q. Jiang, *Adv. Mater.*, 2017, **29**, 1606550.

36 Y. Yao, S.-Q. Zhu, H.-J. Wang, H. Li and M.-H. Shao, *J. Am. Chem. Soc.*, 2018, **140**, 1496–1501.

37 M. Nazemi, S. R. Panikkanvalappil and M. A. El-Sayed, *Nano Energy*, 2018, **49**, 316–323.

38 Z.-Q. Wang, Y.-H. Li, H.-J. Yu, Y. Xu, H.-R. Xue, X.-N. Li, H.-J. Wang and L. Wang, *ChemSusChem*, 2018, **11**, 3480–3485.

39 X.-Q. Wang, W.-Y. Wang, M. Qiao, G. Wu, W.-X. Chen, T.-W. Yuan, Q. Xu, M.

Chen, Y. Zhang, X. Wang, J. Wang, J.-J. Ge, X. Hong, Y.-F. Li, Y. Wu and Y.-D. Li, *Sci. Bull.*, 2018, **63**, 1246–1253.

40 Z.-H. Xue, S.-N. Zhang, Y.-X. Lin, H. Su, G.-Y. Zhai, J.-T. Han, Q.-Y. Yu, X.-H. Li, M. Antonietti and J.-S. Chen, *J. Am. Chem. Soc.*, 2019, **141**, 14976−14980.

41 J. Wang, L. Yu, L. Hu, G. Chen, H. Xin and X. Feng, *Nat. Commun.*, 2018, **9**, 1795.

42 H.-M. Liu, S.-H. Han, Y. Zhao, Y.-Y. Zhu, X.-L. Tian, J.-H. Zeng, J.-X. Jiang, B.-Y. Xia and Y. Chen, *J. Mater. Chem. A*, 2018, **6**, 3211–3217.